# Shock driven instabilities in a varicose, heavy-gas curtain: Mach number effects

by

## Gregory Christopher Orlicz

B.A., Bowdoin College, 2002

THESIS

Submitted in Partial Fulfillment of the
Requirements for the Degree of

Master of Science
Mechanical Engineering

The University of New Mexico

Albuquerque, New Mexico

December, 2007

# Acknowledgments

I am thankful to many people for their respective roles in helping me to complete this journey. Most notably, I'd like to thank my parents for their undying support of me and my decisions. Their expectations and their confidence in me has inspired me to pursue challenges to the best of my ability, and to strive to become a better person. I'd also like to thank my collaborators at Los Alamos. Kathy Prestridge provided guidance throughout the entire process from experimental design to reporting experimental results. Balakumar Balasubramaniam spent several long days with me in the laboratory trying to achieve the 'perfect' data set, and helped me in a countless number of ways during data processing and analysis. Chris Tomkins provided me with very thoughtful feedback and suggestions during the writing process, and I am thankful for his time and attention to detail. I'd also like to thank my thesis advisor, Peter Vorobieff, for his thoughts, wisdom, and instruction, and my classmates at UNM whom with I commiserated during study sessions. Finally, I'd like to acknowledge the important role that my friends have played; whether it be providing encouragement, understanding, or simply a listening ear, I owe them much thanks and appreciation.

# Shock driven instabilities in a varicose, heavy-gas curtain: Mach number effects

by

## Gregory Christopher Orlicz

ABSTRACT OF THESIS

Submitted in Partial Fulfillment of the
Requirements for the Degree of

Master of Science
Mechanical Engineering

The University of New Mexico

Albuquerque, New Mexico

December, 2007

# Shock driven instabilities in a varicose, heavy-gas curtain: Mach number effects

by

## Gregory Christopher Orlicz

B.A., Bowdoin College, 2002

M.S., Mechanical Engineering, University of New Mexico, 2007

## Abstract

A varicose perturbed, thin, heavy–gas curtain is impulsively accelerated by planar shock waves of varying strength and investigated experimentally using concentration field visualization and particle image velocimetry. Two comprehensive experiments were performed with Mach 1.21 and Mach 1.54 incident shock waves at several different times after shock interaction with the initial conditions. Initial condition repeatability allows for visualization of flow feature development over time for both Mach numbers, despite only capturing one post-shock image per run of the experiment. Several features of the flow are identified, qualitatively, as Mach number effects. Integral width versus time, and integral width versus downstream location of the curtain are also reported. Good agreement between integral width experimental data and a mixing width model is demonstrated. Integral width versus downstream location is compared between experiments at Mach 1.21 and 1.54, and can be collapsed using experimental parameters governing the flow. An experiment with a Mach 2.00 incident shock was carried out for the first time in the experimental facility; the resulting image is also reported.

# Contents

*Contents*

# List of Figures

List of Figures

# Chapter 1

# Introduction

## 1.1 Overview

The instability arising at the interface between two fluids of different densities due to the impulsive acceleration of the interface, and the misalignment of pressure and density gradients is known as the Richtmyer-Meshkov (RM) instability [1, 2, 3]. It is a limiting case of the Rayleigh-Taylor [4, 5] instability that occurs when a constant acceleration, such as gravity, acts in the direction from a heavy fluid to a light fluid. Any perturbation that exists at the interface will grow with time, yielding complex nonlinear solutions with even the most simple initial conditions (e.g. a plane sinusoid), eventually inducing mixing of the two fluids. In the RM case, the interface becomes unstable regardless of the direction (i.e. heavy to light or light to heavy) of the impulsive acceleration (e.g. shock wave) [3]. Conversely, any perturbations of a fluid interface in a light to heavy orientation under constant acceleration (e.g. ripples on the interface between water and air in a pond) shrink with time, leading to a stable solution.

While understanding the Richtmyer-Meshkov instability is necessary for insight

into the fundamental physics behind fluid mechanics, it is also of interest for its occurrence in several applications, both practical and naturally occurring, encompassing a range of scales [6]. In inertial confinement fusion (ICF), impulsive compression of the higher density shell into the lower density deuterium-tritium fuel by high energy lasers gives rise to the RM instability and mixing of the shell with the fuel. This impairs the maximum pressure that can be attained, thus limiting the efficiency of the reaction and requiring greater laser input energy than reaction output energy [3, 6, 7]. In supersonic combustion ramjet engines, maximizing the degree of mixing of fuel and oxidizer is of critical importance for combustion rate and improved engine efficiency [3, 6]. Mixing can be enhanced by passing the 'light' hydrogen fuel and the 'heavy' air through an oblique shock wave, thereby producing RM instability. The RM instability is also important in deflagration-to-detonation transition [3, 6]. In nature, it is believed that RM instability plays a large role in the mixing of supernovas as evidenced in Supernova 1987A where the helium and hydrogen layers were observed to be much less stratified than originally predicted, indicating some mechanism of mixing [3, 6]. After the final stage of fusion, a star collapses to its core until it becomes so dense that the infalling matter rebounds, producing a spherical shock wave that propagates outward. As the shock wave propogates through the stratified layers of the dying star, any misalignment of pressure and density gradients produces vorticity, which would serve to enhance the mixing of the remnant gases through RM instability.

The underlying mechanism for amplification of initial perturbations in the RM instability is baroclinic vorticity deposition, generated by the misalignment of pressure (shock wave) and density gradients (fluid interface) [3]. Consider the case of a plane sinuous interface with small initial perturbation amplitude. Initially, after the pressure impulse, vorticity amplifies the perturbations causing the peaks and troughs of the interface to grow linearly in time. As time increases, the peaks and troughs grow asymmetrically, with spikes of heavy fluid penetrating into light, and

bubbles of light fluid penetrating into heavy [3]. When the perturbation amplitude approaches that of the wavelength, the growth is nonlinear. At later times, vorticity causes the spikes to evolve, rolling up into mushroom shaped structures, and the Kelvin-Helmholtz shear instability causes small scale features to appear along the distorting interface [3]. Eventually, this leads to turbulent mixing.

## 1.2  Governing Equations

Taylor first developed a theory to describe the growth of sinusoidal perturbations on an interface between a heavy fluid, of density $\rho_2$, over a light fluid, of density $\rho_1$, in a constant gravitation field using linear stability theory [3, 5, 6]. Given a perturbation of $\eta(x,t) = a(t)cos(kx)$ the perturbation amplitude grows according to

$$a = a_0 cosh(\sqrt{kgAt}) \tag{1.1}$$

where $a$ is the amplitude ($a_0$ is the initial perturbation amplitude), $k = \frac{2\pi}{\lambda}$ is the wavenumber, $g$ is constant acceleration due to gravity, and $A$ is the Atwood number defined as the difference between fluid densities divided by their sum,

$$A = \frac{\rho_2 - \rho_1}{\rho_2 + \rho_1}, \tag{1.2}$$

where $\rho$ is the fluid density, and by convention the acceleration is directed from fluid 2 to fluid 1. Therefore, the Atwood number is positive if acceleration is directed from a heavy to a light fluid.

Thus, in such a system of heavy over light, perturbations grow exponentially with time as long as the interfacial amplitude is small compared to the wavelength, $\lambda$ [1, 6, 8, 9]. In general, this is taken to be the case as long as ka<1 [1, 3, 6]. As the amplitude approaches the wavelength, nonlinearities come into play and this linear

model is no longer valid. Note that if gravity is directed in the opposite direction, the system stabilizes.

Richtmyer expanded upon Taylor's formulation by postulating the growth of initial perturbations of a fluid interface due to an impulsive force [1, 3, 6]. He considered the case of a planar shock wave traveling in a direction normal to the interface from a light to a heavy fluid. If the shock wave is sufficiently weak, fluid incompressibility can be assumed. Richtmyer modelled the problem using Taylor's equations, but substituted gravitational acceleration with a Dirac delta function to capture the impulsive shock [1, 3, 6]. Richtmyer's linear stability theory based formulation then yields a growth rate of the instability

$$\frac{da}{dt} = kAva_0 \qquad (1.3)$$

where $v$ is the velocity imparted upon the interface by the impulsive acceleration. In contrast to constant acceleration, in the impulsive acceleration case the growth rate does not depend on time, and perturbations grow linearly as long as the amplitude is sufficiently small ($ka < 1$) [6], and nonlinearity does not dominate the solution. Although not considered by Richtmyer, growth occurs regardless of the orientation of the fluids (i.e. light to heavy or heavy to light). In the heavy to light case, the initial perturbations first decrease in amplitude, reverse phase, and then continue to grow linearly in the small amplitude regime [3, 6]. Meshkov was the first to confirm Richtmyer's results experimentally, albeit qualitatively, giving rise to the instability's name [3].

The mechanism by which vorticity is generated is derived from the equation for a Navier-Stokes fluid. By taking the curl of the momentum, one obtains the vorticity equation

$$\frac{\partial \vec{\omega}}{\partial t} = -\vec{u} \cdot \vec{\nabla}\vec{\omega} + \vec{\omega} \cdot \vec{\nabla}\vec{u} - \vec{\omega}(\vec{\nabla} \cdot \vec{u}) + \frac{1}{\rho^2}(\vec{\nabla}\rho \times \vec{\nabla}p) + \text{viscous terms}, \qquad (1.4)$$

where $\vec{\omega}$ is the vorticity vector aligned normal to the plane of motion, $\vec{u}$ is the velcity vector of a fluid element, $\nabla\mathrm{p}$ is the pressure gradient (e.g. across a shock wave), and $\rho$ is the density of the fluid at a given location [10, 11]. In the current study, the flow is considered to be two-dimensional, viscous effects are assumed small, and because it is driven by a shock, baroclinic vorticity deposition is considered to dominate. Assuming all terms on the right hand side to be negligent compared to the baroclinic term, the vorticity equation becomes

$$\frac{\partial\vec{\omega}}{\partial t} = \frac{1}{\rho^2}\vec{\nabla}\rho \times \vec{\nabla}p \qquad (1.5)$$

It can be seen that vorticity deposition is maximized when the pressure and density gradients are orthogonal. Comprehensive reviews of the RM instability are presented by Brouillette [3] and Zabusky [11].

## 1.3 Experimental History

Experimentally, the most common way to achieve an impulsive acceleration for study of the RM instability is to produce a travelling shock wave in a shock-tube [3, 6]. In a typical shock-tube, one end of the tube (driver section) is separated with a diaphragm and is pressurized. At a designated pressure, the diaphragm is ruptured and a shock wave begins propogating down the length of the tube (driven section), while an expansion fan begins travelling upstream toward the driver section end wall. As the shockwave travels through the driven section, it becomes planar. At some position downstream (test section), a fluid interface is created and viewports allow for interrogation of the resulting fluid dynamics before and after shock passage. The two most significant obstacles for experimental study of the RM instability are (1) the creation of a well–characterized and repeatable fluid interface, and (2) the implementation of adequate diagnostics.

To address the first problem, the early experiments used fragile membranes to separate two gases and create a well defined, unmixed, single interface (according to reference [6]). The membranes were spread over a very thin wire mesh in a sinusoidal pattern to give the initial perturbation. Upon arrival of the shock wave, the membrane is shattered and the shock wave passes through the interface giving rise to the RM instability. Although the interface is well characterized and repeatable, the use of the membrane introduces new problems [3, 6]. First, fragments from the shattered membrane become entrained in the resulting flow, and it is unclear what effect this has on the fluid mechanics. Often, experiments that have used membranes have reported growth rates that are smaller than those predicted by theory, indicating that the membrane adds an unknown level of complexity to the dynamics of the system [6]. The membrane fragments also complicate visualization of the flow, making it difficult to use planar imaging techniques, and more difficult to attain quantitative information from planar visualization. Membranes were also used in later experiments to create sawtooth perturbations on a single interface [12, 13, 14], and other geometries [15, 16, 17, 18].

Experiments have also used a sliding plate with a sinusoidal perturbation to initially separate the two fluids [19, 20]. Just before the shock is released, the plate is retracted and the shock wave interacts with the interface. However, the motion of the plate drags fluid along with it, causing perturbations on the interface that cannot be controlled. Additionally, some mixing of the two gases occurs before shock impact resulting in a relatively thick, diffuse interface. Therefore, the initial conditions in these experiments are difficult to characterize, and lack repeatability. This not only makes comparison of the experimental results to numerical models and theory a significant challenge, but also inhibits comparison between experiments.

In another experiment, first reported by Jones and Jacobs [21], a new technique for creating a membraneless single interface in a vertical shock tube was developed. In

this experiment, light and heavy gases flow through opposite ends of the tube meeting at some location where slots in the tube walls on opposite sides allow the gases to exit. This leaves behind a nominally flat and relatively thin interface between the gases at the stagnation point of the opposing flows. The shock tube is then oscillated in the horizontal direction at a prescribed frequency using a stepper motor and crank to produce a sinusoidal standing wave for the initial perturbation. This same setup has since been used by others [8, 22] and has achieved growth rate results that are in good agreement with models in the linear regime.

The RM instability has also been studied at a liquid–liquid interfaces [6, 23, 24] and solid–solid interfaces [25, 26]. In both cases, the interface is much more clearly defined than in membraneless gas–gas interface experiments. The Nova laser experiment at Lawrence Livermore National Laboratory employs high powered lasers to ablate a target to produce a strong shock wave (M>10) that travels through a machined solid-solid 2-D sinusoidal interface [25]. Two major difficulties with studying RM instability in solids are that very strong shock waves are needed to make the solids behave as fluids, and visualization of the resulting flow using radiography lacks resolution [6]. In a notable liquid-liquid interface experiment, a sinusoidal interface of light over heavy is formed in a clear tank that is mounted on a pair of vertical rails [23]. The sled is then made to drop onto a coil spring where it rebounds to provide an impulsive accleration. The resulting RMI can then be visualized during the subsequent free fall until the tank impacts the spring for the second time. Because the impulsive force is relatively weak and the Atwood number is low (A=.30 and .15), the development of the RM instability is relatively slow. Slower growth has the advantage of greater ease of visualization, and with the aid of a well defined interface, this experiment yields good comparison with linear growth models after taking into account the finite interaction time with the spring [6]. However, study of the late time nonlinear regime is not possible as the RM instability is still at a relatively early stage upon completion of the free fall of the tank. This experiment was improved

upon later to allow more time for free fall with improved diagnostics and improved interfacial perturbation mode generation [6]. However, well–mixed turbulent states are still beyond the reach of the experiment.

While single interface experiments are desirable test cases for validation of models, other more complex interfacial configurations have been extensively studied. These include spherical soap film bubbles of light or heavy gas in vertical shock-tubes [27, 28], laminar jet cylinders of light or heavy gas [29, 30, 31, 32], and heavy gas curtains with membranes [18] and without [33, 34, 35, 36, 37, 38, 39, 40] in horizontal shock-tubes. In the recent spherical bubble experiments [27, 28], a soap film bubble is created by a retractable injector in air. Once the bubble is formed, the injector releases the bubble and is retracted into the inner wall of the shock-tube so as not to disrupt the flow. The bubble then falls or rises (depending on the density of the injected gas) a certain distance to allow for oscillations of the bubble to die out before a shock wave is timed to impact the bubble within the field of view. In gas cylinder experiments, a laminar jet is flowed out of a nozzle upwards (He) or downwards ($SF_6$) in a horizontal shock-tube, and then impacted by a shock wave. In a recent experiment, the RM instability resulting from five different configurations of heavy $SF_6$ cylinders was studied [32]. Reported were the comparison of integral mixing widths, as well as, for the first time in shock accelerated gaseous flows, the stretching rate of material lines made possible by advanced diagnostics.

In the present study, the interface of interest is a membraneless, varicose, heavy–gas ($SF_6$) curtain flowing in air. This configuration is sometimes referred to as A-B-A, in the sense that one fluid, B, is sandwiched by fluid A, creating two nearby interfaces (first light to heavy and then heavy to light). Its formation is similar to the laminar heavy gas jet cylinder experiments, and relies upon the shape of the nozzle. In both the flowing cylinder and curtain experiments, a small amount of diffusion occurs, resulting in an interface of finite thickness, but in most experiments this effect is

minimized by imaging cross-sections close to the nozzle exit. In the first varicose curtain experiments, 3 distinct flow morphologies were reported from the same nominal initial conditions [33]. Later these morphologies were observed experimentally and shown numerically to be the result of small differences in the initial conditions[34, 41]. Specifically, that the perturbation amplitudes were either slightly greater on the upstream side (upstream mushrooms), downstream side (downstream mushrooms), or nominally equal on both sides (sinuous). The qualitative flow bifurcation in these experiments showed just how sensitive the resulting RM instability is to even very small changes in initial conditions, and moreover emphasized the importance of being able to generate initial condition repeatability with good characterization. This is not a trivial feat when dealing with a free flowing jet curtain, although the initial conditions in the present study are very repeatable, as is discussed in Chapters 2 and 3. With advanced diagnostics that will be described in Chapter 2 they are also well characterized. In the varicose curtain, the existence of two nearby interfaces adds a level of complexity to the dynamics of the RM instability, as the initial perturbations on either side of the curtain do not grow independently, but interact and influence the instability development.

## 1.4 Previous Mach Number Effect Studies

In the present study, multiple experiments were performed on a varicose, heavy gas curtain to observe the effects of the resulting RM instability when the incident shock wave Mach number was varied within the weak shock regime ($M \leq 2$). Some previous studies with a variety of initial conditions have reported results of Mach number variation, but overall, reports regarding Mach number effects in the RM instability are sparse.

One experiment that discusses Mach number effect is reported by Jacobs and

Krivets [22] in which a membraneless single interface between air and $SF_6$ is created using opposing flows that exit from slots in the side of the shock tube. Reported in this study are experiments at three different Mach numbers: Ma= 1.1, 1.2 and 1.3, with nominally the same sinusoidally perturbed initial conditions (results from Ma= 1.1 and 1.2 were first reported in Collins and Jacobs [8]). In this study, it was found that slightly increasing the Mach number of the incident shock effectively increases the duration of the experiment when time is nondimensionalized. In an absolute sense, increasing the Mach number allowed the researchers to observe the RM instability in a more developed state before the reflected shock wave from the end of the shock tube returned to interact with the evolving interface. Perturbation amplitude growth of the single interface was also reported; growth data agreed fairly well with amplitude growth models, and effectively collapsed if amplitude and time were appropriately nondimensionalized. It was also stated that increasing the Mach number from 1.1 to 1.2 effectively caused the interface to develop twice as fast since the interface velocity is a factor of 2 larger in Ma= 1.2, and the amplitude growth is proportional to interface velocity, as given by Richtmyer's linear formula.

Two separate experiments carried out by Ranjan *et al.* discuss results of increasing Mach number for a spherical heavy argon bubble [27], and a spherical light helium bubble [28], both in atmospheric nitrogen. The intent of both studies was to attempt to bridge the gap between high Mach number laser driven experiments (Ma>10) and previous low Mach number, bubble interface, shock-tube experiments. In the Mach 2.88 heavy bubble case, researchers observed a secondary vortex ring that was not previously seen in similar experiments at Mach 1.3 or lower, but was previously predicted. The researchers suggest that this feature may result due to differences in compressibility effects when the particle velocity behind the incident shock wave becomes supersonic, which occurs at Mach 2.07 in nitrogen at atmospheric temperature. Similarly, in the Mach 2.95 light bubble experiment, secondary and tertiary counter-rotating vortex rings in the flow field were observed for the first time that

were absent in the previous experiments carried out at Ma<1.3. These features caused the rate of bubble elongation (integral width) to be twice that of the previous low Mach number studies. The researchers attribute these additional flow features in the higher Mach number light bubble experiment to more complex shock refraction and reflection phenomena occuring with stronger incident shocks.

In the solid–solid sinusoidal machined interface Nova laser experiments, Holmes *et al.* [25] report results from negative Atwood number experiments with incident shock Mach numbers of 10.8 and 15.3. It was found that absolute perturbation growth rate increases with Mach number; however, if the growth rates are nondimensionalized by experimental parameters, they reduce with increasing Mach number. This result is confirmed by simulations and models in the report. The nondimensional growth rate reduction is attributed to higher compression of the geometric perturbations at the interface, and resulting changes in the post-shock Atwood numbers as Mach number is increased.

Another experiment reported by Sadot *et al.* [13] investigates the RM instability resulting from a sawtooth perturbed air/SF$_6$ interface that is initially separated by a membrane. Two experiments were carried out, one with large initial perturbation amplitudes and low Mach number (Ma=1.2), and the other with small initial amplitudes and moderate Mach number (Ma=2). Because both parameters were changed between experiments, it is unclear what conclusions can be drawn. Measured in both experiments was the amplitude of the bubble flow feature. In the low Mach number, high amplitude experiment the growth rate of this feature remained positive, but in the moderate Mach number experiments, the growth rate became negative. The researchers attribute this negative growth rate to pressure fluctuations in front of the bubble due to shock reverberation. Yet, it is concluded that altering the perturbation amplitude is the dominant explanation for flow feature differences between the two experiments. Another Mach number study was reported by Bliznetsov *et al.* [16],

in which single interface initial conditions of unreported geometric characterization with both helium/$SF_6$ and air/$SF_6$ configurations were accelerated by shocks ranging from Mach 2 to 9. It was simply reported that higher Mach number shocks cause higher fluid interface velocities and higher mixing width growth rates.

Some of these experiments discuss interesting results related to Mach number effect, but they lack either comprehensiveness, or flow complexity. The current study presents a comprehensive investigation of experiments carried out at two Mach numbers for the first time in a varicose perturbed, membraneless heavy gas curtain, yielding differences in complex flow features on multiple scales. Chapter 2 contains a description of the experimental facility, and Chapter 3 presents the results of the investigation.

# Chapter 2

# Experimental Facility and Diagnostics

The present study was carried out at the horizontal gas shock-tube facility at Los Alamos National Laboratory. The shock-tube has a 75 by 75 millimeter square cross section with a total length of approximately 5.4 meters as seen in Figure 2.1. All but the driver section is open to atmosphere. In general, to create the shock wave, a polypropylene diaphragm is first placed in between the driver and driven sections. Then, compressed gas is flowed into the driver section until the desired pressure is reached (experimentally: 15 psig for Mach 1.21, 50 psig for Mach 1.54, and 150 psig for Mach 2.0). At that time, a signal is sent to cause a solenoid driven set of razor blades to rupture the diaphragm, thus releasing the pressure and causing a planar shock wave to form shortly downstream of the diaphragm location. As the shock wave moves downstream toward the initial conditions, four separate pressure transducers measure the variations in pressure to allow for measurement of shock speed and to trigger imaging diagnostics.
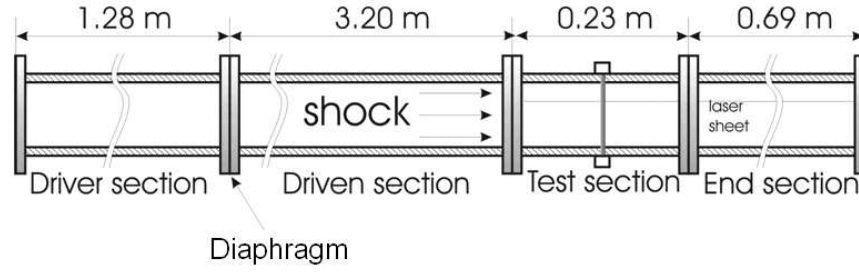
Figure 2.1: Shock tube schematic

## 2.1 Initial Conditions

The initial condition in the present study is a thin varicose sulfur hexafluoride ($SF_6$) gas curtain. To create the initial condition, a settling chamber located above the test section is filled with $SF_6$. Before the shock wave is released, a valve is opened to allow a gravity driven flow of $SF_6$ (as it is heavier than air) from the settling chamber through the nozzle, and into the test section (Figure 2.2). Porous, flow straightening foam is also placed just before the nozzle to help ensure laminar flow. The nozzle itself consists of a single row of closely spaced holes of S/D=1.17, where the spacing, S, is 3.5 mm, and the diameter, D, is 3.0 mm. As the $SF_6$ flows out of the nozzle and into the test section (see photograph taken from the end of the runout section in Figure 2.3), diffusion takes place between the cylinders, thus giving rise to a varicose perturbed $SF_6$ curtain in atmospheric air. At the bottom of the test section, a mild, variable suction exhausts the $SF_6$ out of the shock tube and prevents overflow. The vertical flow velocity ($\approx 0.1$ m/s) can be neglected as it is small compared to the horizontal velocity of the shock-induced dynamic flow ($>100$ m/s). Therefore, it is reasonable to assume that the flow in the visualization plane after shock impact is nominally two–dimensional for the entire duration of the experiment($<1000~\mu$s).

Experimentally, it was found that if air could be entrained to flow passively on
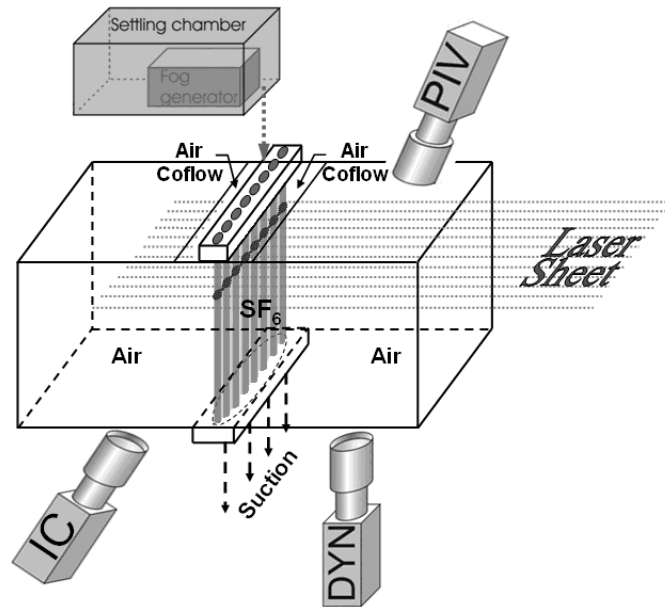
Figure 2.2: Test section schematic showing initial conditions and coflow. When fired, the shock wave will move from left to right.



Figure 2.3: Photograph of the axis view of the shock tube (looking through the window at the end of the end section) showing the varicose curtain initial conditions flowing from top to bottom. Visualization was accomplished with fog droplets for flow seeding in the $SF_6$ and a flashlight for illumination.
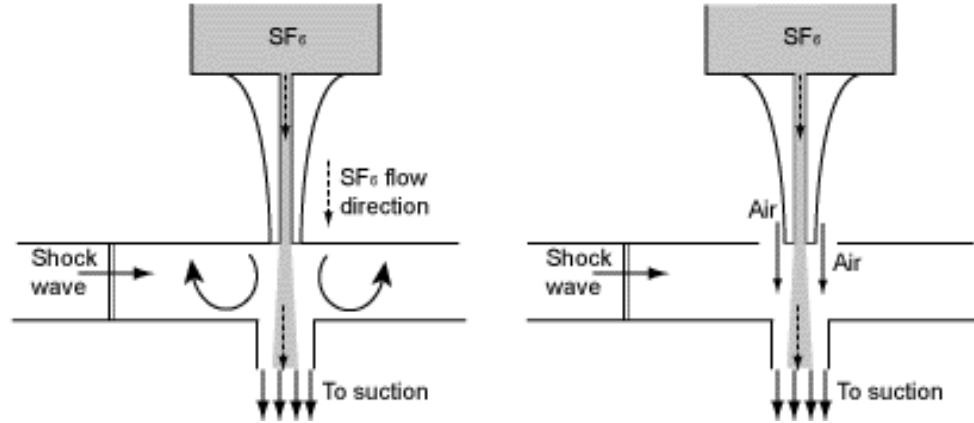
Figure 2.4: *Left*, flowing $SF_6$ induces circulation patterns in air on either side of the curtain leading to streamwise instability; *right*, the suction induces the air to flow alongside the curtain continually passing through the test section.

either side of the $SF_6$, the curtain could be made much more stable. If air was not entrained, then drag from the $SF_6$ flow caused the air within the test section to form circulation patterns, thus causing the curtain to oscillate in the streamwise direction (see Figure 2.4). These unsteady oscillations led not only to unrepeatable initial conditions, but also to asymmetry within individual experimental runs. The nozzle was thus modified to create gaps adjacent to the curtain through which external air would enter, forming a passive coflow nozzle. To ensure laminar entrainment of the air, and thus a symmetric and repeatable $SF_6$ curtain, the bottom of the nozzle was designed with a smooth concave curve on two sides so that the nozzle itself was thinner than the opening to the test section at the insertion point. Given the level of complexity of such a part, stereolithography was found to be the ideal manufacturing method. The nozzle was custom fabricated by an outside company (Harvest Technologies Inc.) using the stereolithography process in which a liquid resin is hardened layer by layer upon laser contact. This allows for the manufacture of virtually any shaped plastic part given a properly formatted CAD drawing, and it met the design criteria well (see Figure 2.5 for a photograph of the nozzle).
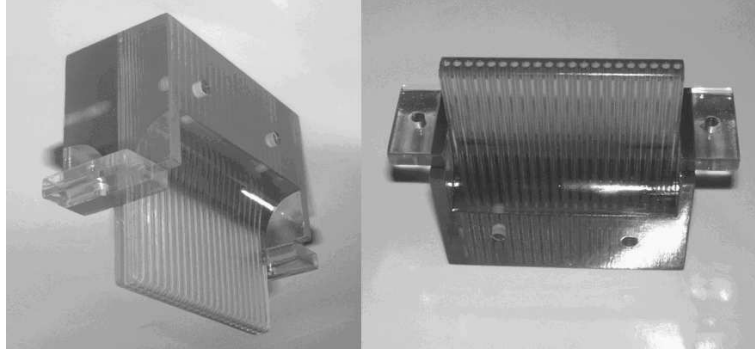
16

Figure 2.5: Two photographs of the nozzle created by stereolithography and used in the experiment. The narrow section with the row of holes is inserted downward into the test section. The curved surfaces allow for smooth entrainment of surrounding air for coflow stabilization.

## 2.2   Imaging Diagnostics

The initial conditions and the dynamic flow evolution after shock passage are visualized using planar laser induced fluorescence (PLIF) with acetone vapor as the tracer. To seed the $SF_6$ with acetone, $SF_6$ is bubbled through liquid acetone in a temperature controlled bath set to 20°C prior to reaching the settling chamber. The bath is set below room temperature to prevent subsequent condensation of the acetone vapor. For visualization, a neodymium-doped yttrium aluminum garnet (Nd:YAG) frequency quadrupled pulsed laser is formed into a thin sheet (<1 mm) using a combination of mirrors, and cylindrical and spherical lenses. The laser output peaks at 266 nm (ultraviolet), at about 12 mJ/pulse with a pulse width of about 10 ns. The ultraviolet (UV) light sheet causes the acetone tracer to fluoresce between 350 nm and 550 nm with a peak at ≈400 nm (in the visible range) allowing for visualization. The acetone vapor tracks the $SF_6$ at a molecular level, giving rise to very high quality, high resolution images representative of $SF_6$ concentration. Acetone also has a phosphorescent signal in response to the laser pulse that occurs on a longer time scale than the fluorescent signal. However, oxygen from the surrounding air that has

17

diffused into the curtain quenches the phosphorescence signal, and blurring of the post-shock flow visualization images is avoided despite the high convective velocity.

The horizontal laser sheet enters the shock tube through a UV–transparent window at the end of the end section, as seen in Figure 2.1, and is positioned to visualize cross section images of the curtain about 2 cm below the nozzle exit. Two individual laser heads provide one pulse each for each experimental run. In general, one pulse is used for illuminating the initial conditions about 5 $\mu$s before shock impact, and the other pulse creates a post-shock dynamic image of the developing vortical structure at a specified time. Both laser heads are triggered off the rise in the signal (associated with the passing shock wave) from the pressure transducer imbedded in the wall of the shock tube that is located immediately upstream of the test section. Two more pressure transducers located further upstream serve to measure shock velocity, and a fourth, positioned downstream at the initial condition location, measures the time of shock impact.

The images are then captured using 2 separate 16-bit, cooled, back-illuminated Apogee charge-coupled device (CCD) cameras. The camera that captures the fluorescence from the initial condition pulse, labeled 'IC' in Figure 2.2, has a 2184 X 1470 CCD but is 3 X 3 binned on the chip to increase signal intensity, yielding a 728 X 490 image. The IC camera is also slightly tilted as shown in Figure 2.2 to gain optical access to the initial conditions. The dynamic camera, labeled 'DYN' in Figure 2.2, is oriented orthogonally to the plane of the laser sheet, and has an unbinned 1024 X 1024 CCD. Both the IC and the dynamic camera provide high resolution images: about 52 $\mu$m/pixel and 54 $\mu$m/pixel, respectively. The shutters for both cameras are relatively slow, and therefore are triggered to open just before the signal that triggers the solenoid driven blades to begin the dynamic experimental run with the rupturing of the diaphragms. Each shutter remains open for 2 seconds before closing. Background images are also captured periodically and then subtracted out of each resulting image. The processed image gives the intensity of fluorescence from

the acetone vapor, which scales linearly to $SF_6$ concentration, yielding a 2-D $SF_6$ density map.

Although it is widely accepted that PLIF is an non-intrusive imaging technique, it was discovered in this experiment that illuminating the initial conditions could alter the dynamic flow. When the IC laser pulse was fired with peak power shortly before shock impact, and focused at the initial conditions, the resulting dynamic structures appeared more blurred at later times, indicating that the initial conditions were altered. In-depth discussion of this topic is beyond the scope of this paper, and will be an object of further study, but some notes and a visual illustration can be found in Appendix A. To minimize this effect while still capturing the initial conditions, the power of the IC laser pulse was reduced until within a range where the dynamic images did not appear to be blurred. As a consequence, the signal to background noise ratio of the IC camera images was decreased from approximately 14, when at maximum power, to 4. The dynamic laser pulse remained at maximum power.

Experiments were performed with incident shock waves of Mach 1.21 and 1.54 to capture dynamic images at several different times using PLIF, yielding data sets of two–dimensional density maps for each Mach number. After a given data set was complete, several experiments were performed using particle image velocimetry (PIV) and PLIF within the same experimental run to get a measure of the velocity field and the density field simultaneously at two different times with the given Mach number. This was accomplished using a second Nd:YAG pulsed laser that is frequency doubled, operating at 532 nm (green) and formed into a thin laser sheet. Beam combining optics were set to align both the PLIF laser and the PIV laser in the same plane to ensure imaging of the same dynamic event. In addition to acetone vapor, the $SF_6$ was seeded with glycol/water droplets ( .5 $\mu$m in diameter on average) from a theatrical fog machine within the settling chamber, and then allowed to flow into the test section. Triggered off the same pressure transducer, the PIV laser

was timed to provide two pulses 5 $\mu$s apart, one on each side of the single dynamic PLIF laser pulse, to get a measure of the velocity field at the moment of the PLIF image, and to reduce any noise that may arise due to simultaneous PLIF and PIV laser pulses. The green light from the PIV laser is scattered off the fog particles and captured in two separate images taken by a single buffered camera, labeled 'PIV' in Figure 2.2, so that only one pulse is captured in each frame. The two resulting images, closely spaced in time, are then processed using cross correlation software to derive velocity vectors.

The PLIF data is captured the same way as described above. A low band pass filter in front of each PLIF camera lens prevents the relatively higher wavelength green PIV laser light from reaching the CCD. Fog visualization for species concentration measurement is inferior to acetone PLIF in that the fog droplets fail to follow the diffusion of the $SF_6$ in the initial conditions, and lag behind the initial impulsive acceleration of the $SF_6$ curtain. However, once the droplets are accelerated, they accurately trace the flow for velocity field measurements [37, 39].

## 2.3 Mach Number Variability

In the present study, the evolution of the RM instability is compared between experiments at different Mach numbers with nominally identical initial conditions. Varying the Mach number is accomplished in two ways that are practical in the current experimental facility: varying the driver pressure, and changing the driver gas. To attain increasing Mach numbers, the required driver pressure increases exponentially for a given driver gas, but the shock speed is also determined by the specific heat ratio, $\gamma$, of the driver gas. The pressure that is required to reach a given Mach number

changes according to the following equations [10]:

$$M_s = \sqrt{\frac{(\gamma_1 - 1) + (\gamma_1 + 1)(p_2/p_1)}{2\gamma_1}} \tag{2.1}$$

where $M_s$ is the desired Mach number, $p_1$ and $p_2$ are the pressures ahead of the shock wave (atmospheric pressure) and behind the shock wave, respectively, and $\gamma_1$ is the specific heat ratio of the atmoshperic air. Then,

$$\frac{p_2}{p_1} = x = \frac{2\gamma_1 M_s^2 - (\gamma_1 - 1)}{\gamma_1 + 1} \tag{2.2}$$

Finally, the driver pressure, $p_4$, required to achieve $M_s$ is,

$$p_4 = p_1 x \left[ 1 - \frac{(\gamma_4 - 1)(\frac{a_1^*}{a_4^*})(\frac{p_2}{p_1} - 1)}{\sqrt{2\gamma_1[(\gamma_1 - 1) + (\gamma_1 + 1)(\frac{p_2}{p_1})]}} \right]^{\frac{2\gamma_4}{\gamma_4 - 1}} \tag{2.3}$$

where $\gamma_4$ is the specific heat ratio of the driver gas, and $a_1^*$ and $a_4^*$ are the speed of sounds in the atmospheric air and the driver gas, respectively, defined as

$$a^* = \sqrt{\gamma R T/m}, \tag{2.4}$$

where $R = 8.314 J/(mol * K)$ is the gas constant, $T$ is the temperature, and $m$ is the molecular mass in kilograms per mol. This yields 346 m/s for the speed of sound in air at room temperature. From the equations above, it can be shown that the higher the $\gamma$ of the driver gas, the less pressure is required to achieve the same Mach number. Traditionally, the shock tube at Los Alamos has operated at M= 1.2 using nitrogen as the driver gas with $\gamma_{N_2} = 1.4$, but helium has $\gamma_{He} = 1.67$, making it more desirable to be used as a driver gas to achieve higher Mach numbers. In Figure 2.6 the curves for Mach number versus required driver gauge pressure are given for both nitrogen and helium at 7100 ft, which was determined to be the elevation of the experimental facility in Los Alamos using a hand held GPS unit. At 7100 ft and

room temperature, the atmospheric pressure, $p_1$, is approximately 11.46 psi. It can be seen that the effect of varying $\gamma$ is significant. For example, to achieve Mach 2.0, the required driver gauge pressure for nitrogen is approximately 360 psig, while it is only approximately 100 psig for helium. Therefore, helium was chosen for the driver gas in the current study, as for a given Mach number, it would lower the material stresses in the shock-tube and for promote personal safety (the shock-tube has a maximum allowable driver gauge pressure of 350 psig based on pressure safety reviews).
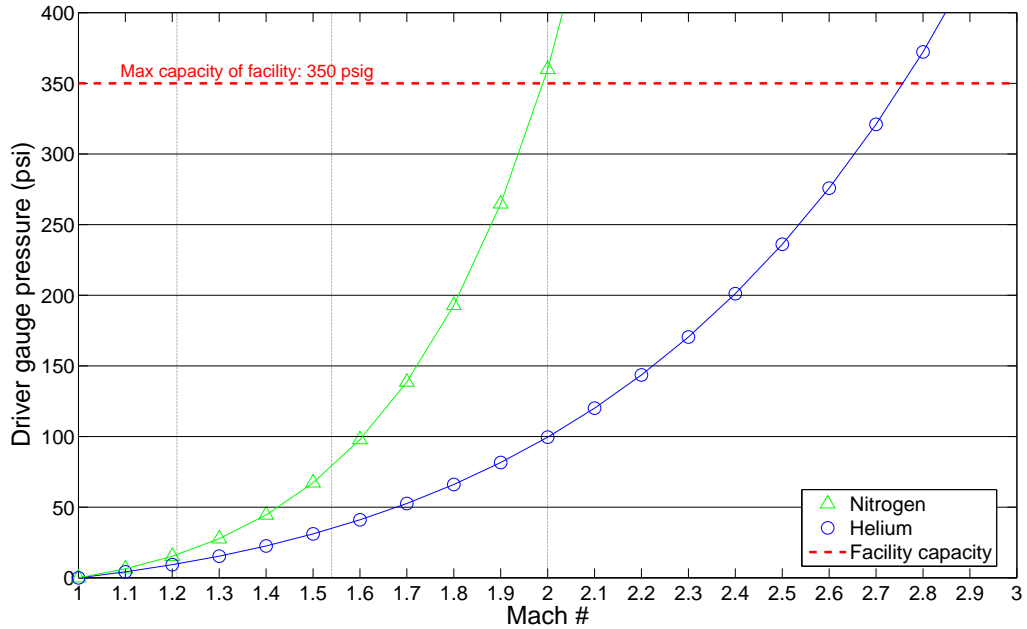


Figure 2.6: Mach number vs required driver pressure for nitrogen and helium. Maximum allowable pressure for the facility is 350 psig. Vertical lines represent Mach numbers of shock waves from the current experiment: Ma = 1.21, 1.54, and 2.00.

In summary, the experimental facility allows for studying the interaction of shock waves, ranging from Mach 1 to Mach 2, with stable, repeatable initial conditions visualized by PLIF. Diagnostic imaging of the resulting RM instability includes both PLIF and PIV, allowing for the measure of two-dimensional density and velocity fields simultaneously.

# Chapter 3

# Results

As was discussed in Chapter 2, only two PLIF laser pulses are available for each run of the experiment. Therefore, to see how the RM instability evolves over time, many runs of the experiment must be carried out, with varying pulse time between shots. In general, one of the available pulses is used to image the initial conditions, allowing for only one dynamic image to be captured per experimental run. In this way, several experiments are performed to get a set of images at a particular time after shock impact. Then the laser pulse timing is varied, and another set of images is captured at a different time, and so on. Figure 3.1 shows the number of shots reported in the current study at each time for experiments at Mach 1.21 (420 m/s) and Mach 1.54 (532 m/s). With multiple images from different runs of the experiment at multiple times after shock impact, two sets of time sequenced images were compiled from this data to visualize the evolution of the single-mode, varicose, $SF_6$ gas curtain in air for experiments at Mach 1.21 and Mach 1.54. Additionally, two runs of the experiment were carried out at Mach 2.00 (692 m/s) measuring the density field at a single time. In both Mach 1.21 and 1.54 experiments, the timing of the dynamic pulse[0] was varied from just after shock impact to as late in time as could be imaged within

---

[0]triggering image capture

the test section. For Mach 1.21, this corresponded to t=915 $\mu$s, where t=0 is the time of incident shock impact, and for Mach 1.54, it was t=465 $\mu$s. Also in both data sets, some early time dynamic images were captured with the IC camera, as its field of view included about 12 mm upstream of the initial condition location. Such images were achieved at the expense of not capturing the initial conditions for those experimental runs.

| Time (microseconds) | Camera | Number of Runs |
|---|---|---|
| 15 | IC | 1 |
| 55 | IC | 1 |
| 65 | IC | 1 |
| 75 | IC | 1 |
| 85 | IC | 1 |
| 95 | IC | 1 |
| 265 | DYN | 6 |
| 315 | DYN | 4 |
| 365 | DYN | 7 |
| 415 | DYN | 11 |
| 465 | DYN | 6 |
| 515 | DYN | 7 |
| 565 | DYN | 6 |
| 615 | DYN | 4 |
| 665 | DYN | 13 |
| 715 | DYN | 4 |
| 815 | DYN | 2 |
| 915 | DYN | 2 |

(a)

| Time (microseconds) | Camera | Number of Runs |
|---|---|---|
| 5 | IC | 1 |
| 15 | IC | 2 |
| 20 | IC | 1 |
| 25 | IC | 1 |
| 30 | IC | 1 |
| 35 | IC | 1 |
| 40 | IC | 1 |
| 45 | IC | 1 |
| 100 | DYN | 1 |
| 115 | DYN | 6 |
| 140 | DYN | 4 |
| 165 | DYN | 4 |
| 190 | DYN | 2 |
| 215 | DYN | 5 |
| 225 | DYN | 1 |
| 265 | DYN | 7 |
| 315 | DYN | 11 |
| 365 | DYN | 6 |
| 415 | DYN | 7 |
| 465 | DYN | 4 |

(b)

Figure 3.1: Tables showing times of dynamic images, the camera used, and number of shots taken at each time after shock impact for (a) Mach 1.21 data: 72 total runs, and (b) Mach 1.54 data: 59 total runs.

In order to ensure that the initial conditions were nominally the same between the Mach 1.21 and Mach 1.54 experiments, several shots were taken with a Mach 1.54 shock immediately prior to performing the set of Mach 1.21 experiments. These dynamic validation images matched those that were taken during the earlier Mach 1.54 data set within the degree of variability seen in the earlier experiment itself, confirming initial condition similarity. Additionally, to ensure that the initial conditions remained the same within a day, shots were taken periodically with timings that matched those taken earlier in each data set. Dynamic images are highly sensitive

to the initial conditions as small differences get amplified after shock impact. Therefore, monitoring the similarity of dynamic images can provide more information on IC repeatability than can the IC images themselves, which are also inspected in real time.

Several attempts were made to quantify the degree to which initial conditions matched, using two-dimensional correlation codes, but several issues with the data prevented accurate determination of actual $SF_6$ correlation. The signal intensity to background noise was low in the initial condition images, as mentioned earlier, and the laser power itself inherently has a degree of variability from pulse to pulse. The initial condition camera also sometimes was moved slightly during the course of the experiment. It was not known when camera movement occurred while taking the data, so calibration images were not taken at each camera position, further complicating quantitative correlation. It is believed that the camera movement occurred due to vibrations from the shock-tube during dynamic operation, and that this problem can be mitigated in future experiments. These experimental constraints and errors in imaging limited the ability to meaningfully quantify subtle differences in the IC's, but experience has shown that investigation of the differences between dynamic images can be more rigorous.

## 3.1 Pressure Trace and X-T Diagram Discussion

Using helium as a driver gas allows for higher Mach numbers with less driver pressure, but the expansion fan from the opposite end of the shock tube arrives at the test section much more quickly. In this facility, according to theoretical calculations, this event occurrs at t=945 $\mu$s and t=740 $\mu$s for Mach 1.21 and 1.54, respectively. The interface moved past the test section field of view by that time, and there was no experimental evidence that the expansion fan ever interacted with the evolving

curtain, based upon its steady convection velocity and a lack of an unexpected change in flow evolution. Additionally, the structures were out of the field of view in each case before the shock wave encountered the test section for a second time (reshock wave) after rebounding off the end wall of the end section. Figures 3.3, 3.5, and 3.7 show X-T (position versus time) diagrams with shock waves, reflected shock waves, and expansion fans, for M= 1.21, 1.54, and 2.0 generated using code developed at the University of Wisconsin and altered to the specifications of the experimental conditions in the current study. Figures 3.2, 3.4, and 3.6 show the experimental pressure traces from the four pressure transducers in a representative run, or shot, of the experiment at each corresponding Mach number.

Indicated in each X-T diagram is the location of the initial conditions within the test section and an overlay of the rise in each pressure transducer signal (squares) giving the general space-time of an experimental run. It can be seen that the rises in the signals of the pressure transducers agree very well with the computational code for the incident shock, but that the correlation falls off for the reflected shock wave. This divergence can probably be explained by losses that occur in the experiment that are not accounted for in the idealized code as the experimentally measured reflected shock wave is slower than that according to ideal theory. It is hypothesized that most of the losses occur due to openings in the test section and along the shock tube. It is also likely that other losses occur at the end wall where the shock wave is not perfectly reflected in the experiment. It should be noted that the timing of the reshock wave is not clear from the trace on pressure transducer 4 (IC location) in the Mach 2.0 experiment. The pressure transducers did not have enough sensitivity or resolution to accurately determine the arrival of the expansion fan at their locations.
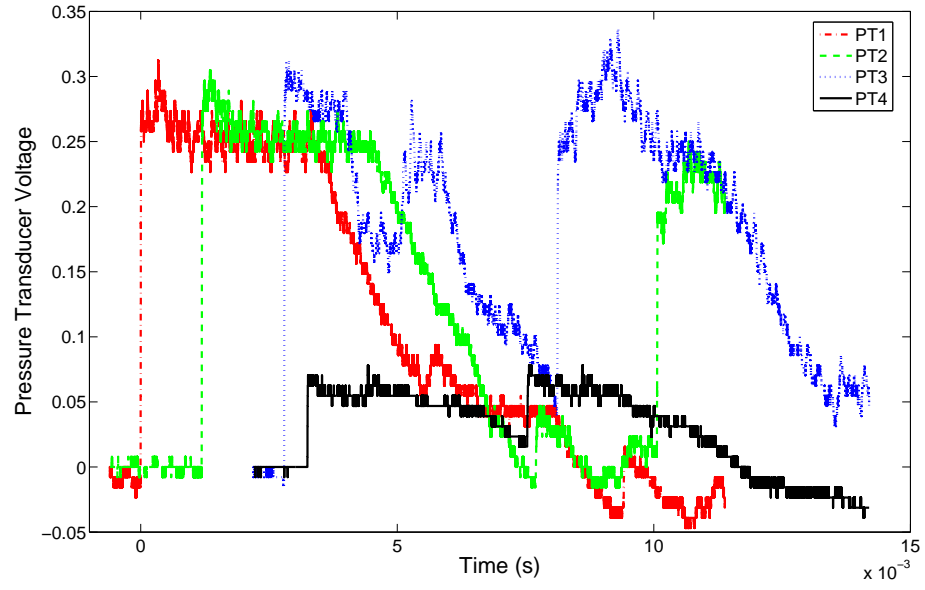
Figure 3.2: Pressure transducer signals from a Mach 1.21 shot

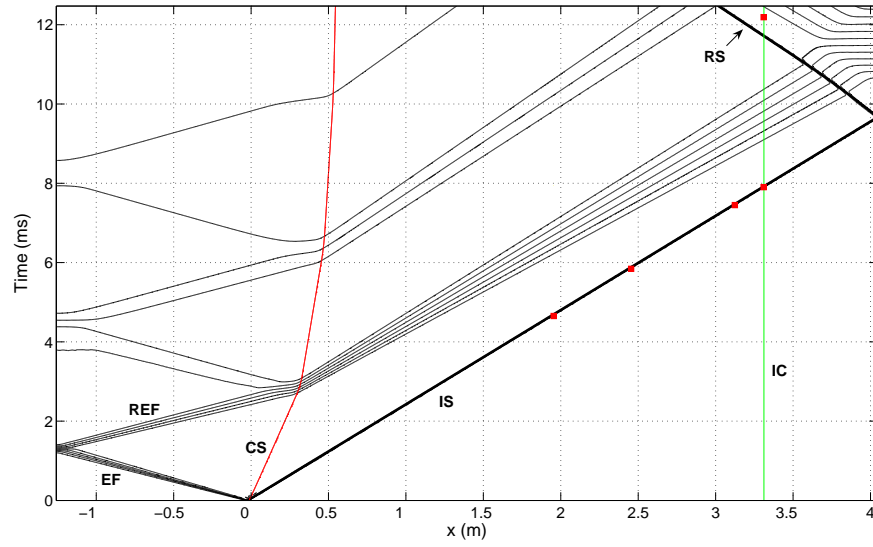

Figure 3.3: Theoretical X(m)-T(ms) wave diagram for Mach 1.21 [42] with experimental pressure trace rises overlaid (squares). X=0 is the location of the diaphragm. IS, incident shock; RS, reflected shock; EF, expansion fan; REF, reflected expansion fan; CS, contact surface; IC, location of initial conditions
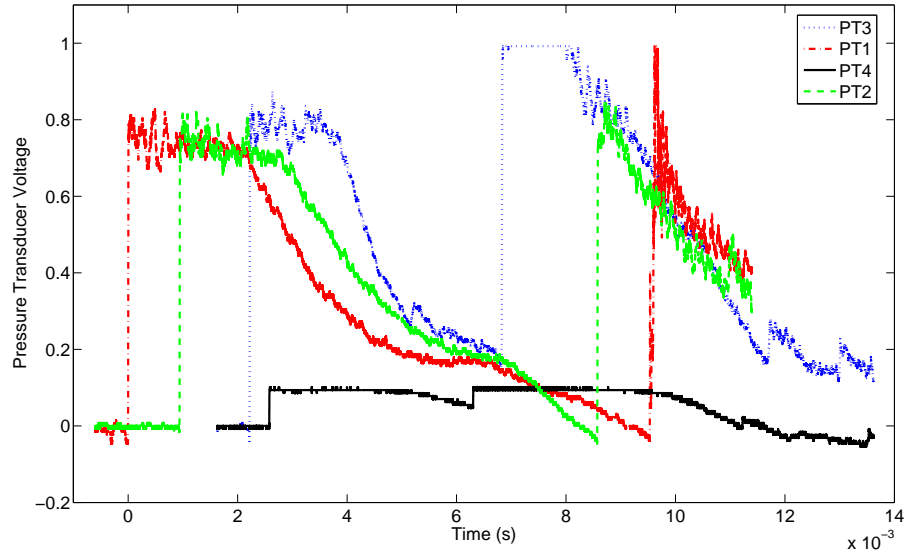
Figure 3.4: Pressure transducer signals from a Mach 1.54 shot



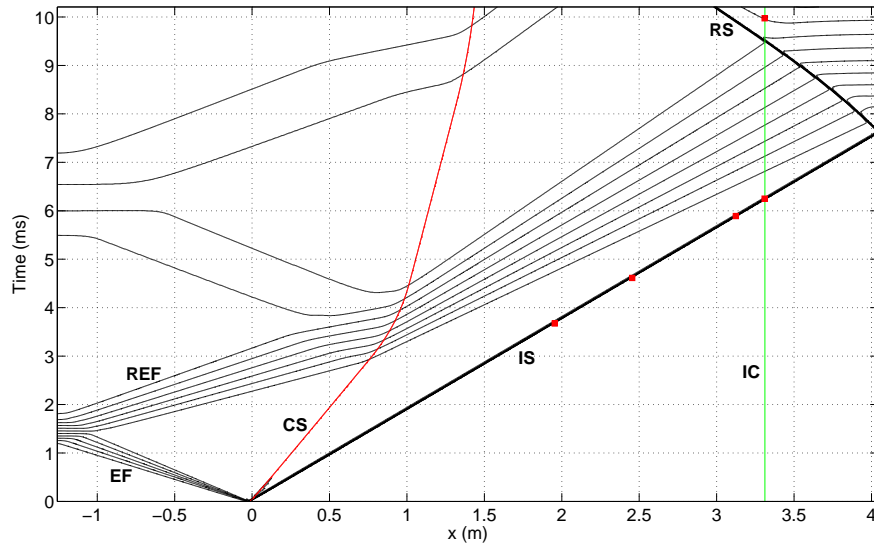Figure 3.5: Theoretical X-T diagram for Mach 1.54 [42] with experimental pressure trace rises overlaid.
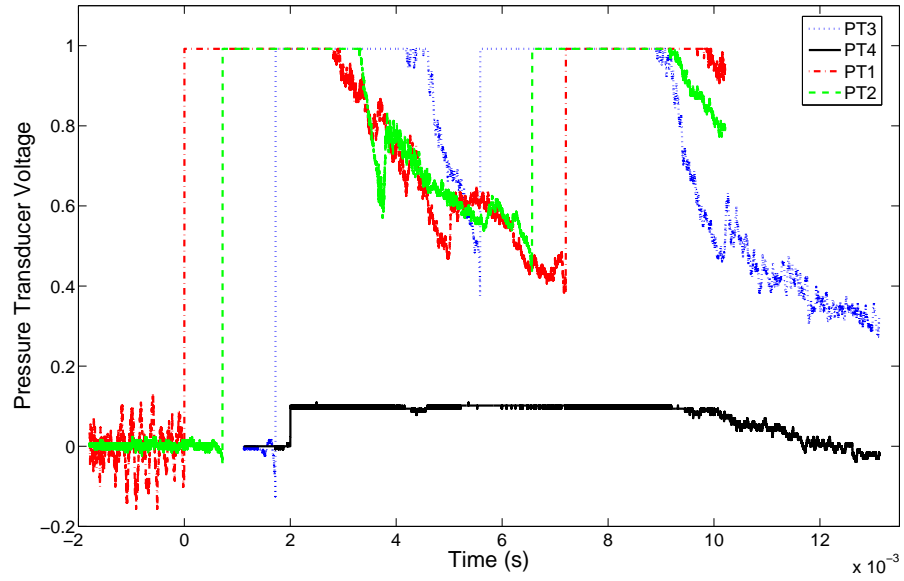
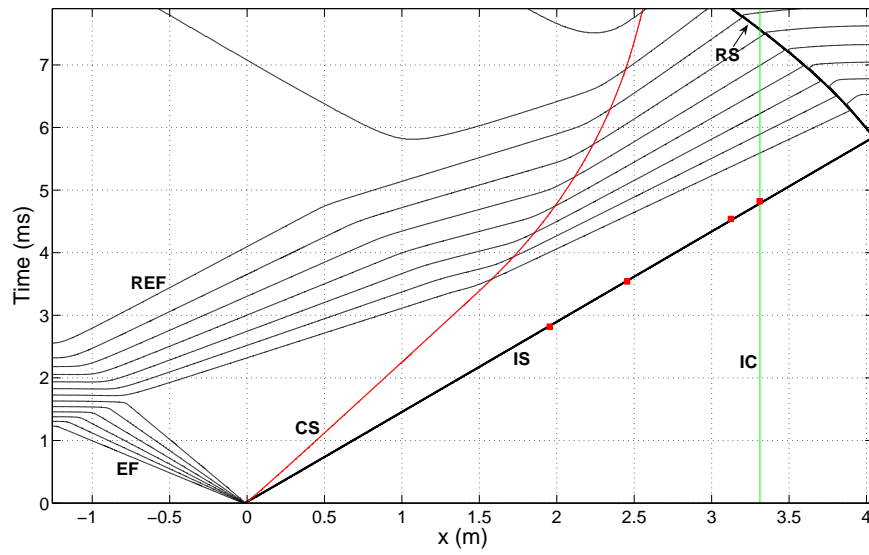Figure 3.6: Pressure transducer signals from a Mach 2.00 shot



Figure 3.7: Theoretical X-T diagram for Mach 2.00 [42] with experimental pressure trace rises overlaid.

*Chapter 3. Results*

Experimentally, it was found that to generate Mach 1.21, Mach 1.54, and Mach 2.00 incident shock waves, driver pressures of approximately 15 psig, 50 psig, and 150 psig, respectively, were required. These values contrast with the calculated theoretical values of 10.02 psig, 34.64 psig, and 99.49 psig. Therefore, the theoretical required driver pressure was consistently about 70% that of the experimentally determined driver pressure in each experiment. It is believed that this was mainly due to several losses incurred during the shock generation process, including the imperfect rupture of the diaphragms, and boundary layer effects. Also, the solenoid-driven razor blades take up a significant cross section of the driver section near the diaphragm location, and this imperfect transition from driver section to driven section could be the cause of additional mechanical losses as the pressure waves initially form into a shock wave.

Some of the discrepancy also results because air is not evacuated from the driver section prior to pressurizing above atmospheric pressure with helium, so the driver gas consists not only of helium, but also a small fraction of air. Because the specific heat ratio of air ($\gamma$=1.4) is smaller than that of helium ($\gamma$=1.67), the operating specific heat ratio is really a weighted average of the two gasses, having the effect of increasing the required driver pressure in the experiment above what is calculated for pure helium. In previous experiments using nitrogen ($\gamma$=1.4) as the driver gas with the same experimental setup (not reported here), a driver pressure of 20.5 psig was required for the generation of a Mach 1.21 shock wave, while only 16.36 psig is required according to ideal theory. Because nitrogen and air have the same specific heat ratio, and because there is only a small difference in the speed of sound between $N_2$ and air, the losses in the case of nitrogen as the driver gas can only be explained by the mechanics described earlier. Since the theoretical driver pressure for nitrogen is about 80% that of the experimental value, and for helium it is about 70%, it is speculated that the extra 10% error in the helium case is a result of not using the weighted average of the specific heat ratio in calculations. In this interpretation, the remaining discrepancy of approximately 20% is due to the mechanisms listed above.

In Figure 3.6, the trace from pressure transducer 1 (PT1) shows a significant oscillatory signal above background noise ahead of the incident shock wave. In Mach 2.0 experiments, about 10 individual sheets of polypropylene diaphragm were stacked at the diaphragm location to prevent premature rupture of the diaphragms due to the high pressure in the driver section (5 sheets were used in Mach 1.54 experiments, while only one was required for Mach 1.21). It is proposed that during the finite time it takes for all diaphragms to rupture in the Mach 2.0 case, a sound wave is generated in air that begins to propagate down the length of the shock tube before the shock wave is formed. One possible mechanism for this could be a drum-like effect, wherein a pressure wave from the driver section generated from the rupture of one diaphragm collides with a subsequent unruptured diaphragm. Since the diaphragms are all taut under pressure, this pressure wave could have an effect like beating on a drum in the instant before the subsequent diaphragm is ruptured itself. Because the signals on the other pressure traces before shock arrival are either much smaller or nonexistent, it is believed that the shock wave catches up to, and consumes, these sound waves prior to arriving at the initial conditions.

## 3.2   Time Series Comparison

The fluid dynamics in the current study are dominated by pairs of closely spaced, interacting vortices generated through baroclinic vorticity deposition. As the initial amplitudes on either side of the curtain grow dependently, the vorticity rolls up and distorts the fluid interfaces to interact with adjacent vortices, giving rise to complex flow features that are highly dependent upon the initial conditions. The growth of initial perturbations should also be nonlinear for the entire duration of the experiment not only because of interaction between the two closely spaced interfaces, but also because the initial amplitudes ($a_0$) on both interfaces are on the same scale as the

wavelength of the perturbations ($ka_0 \approx 1$). Due to the diffuse interface, a precise definition of $a_0$ is somewhat subjective in the current study as it depends upon the selection of a threshold. This complicates comparison to the available models that assume interfaces to be discontinuous.

The flow evolution can be seen in Figure 3.8, where a time series for both the Mach 1.21 and the Mach 1.54 data sets is compiled. Each image in the time series corresponds to a separate individual run of the experiment, and due to small differences in the initial conditions, small scale features do not always register from frame to frame. However, the highly repeatable nature of the dynamic images in the present study suggests that the initial conditions were more repeatable than those for any previously reported thin heavy gas curtain. This allows for the tracking of large scale features and some small scale features through their development in time. Figure 3.9 shows two sets of three images at dynamic times of t=215 $\mu$s and t=315 $\mu$s from different runs of the Mach 1.54 experiment, and demonstrates the remarkable repeatability of the current study even at later times when mixing in the vortex cores is occurring, and flow complexity is high. The data sets used to generate the time series comprise several images at most times, corresponding to different individual runs of the experiment (as shown in Figure 3.1). With multiple shots to choose from at most times, images for the time series in Figure 3.8 were selected based on qualitative registering of flow features, and symmetry within the individual image.

It can be seen in Figure 3.8 that the flow morphology for Mach 1.21 and Mach 1.54 is fairly similar on large scales at early times, although the growth of the initial perturbations occurs faster in Mach 1.54 experiments, as one would expect, due to the greater amount of vorticity deposited on the initial conditions upon shock impact. For example, compare the similarities between the amount of development at t=265$\mu$s for Mach 1.21 and t=115$\mu$s for Mach 1.54, as indicated by double headed arrows in Figure 3.8. Also, compare images at t=415$\mu$s for Mach 1.21, and t=165$\mu$s
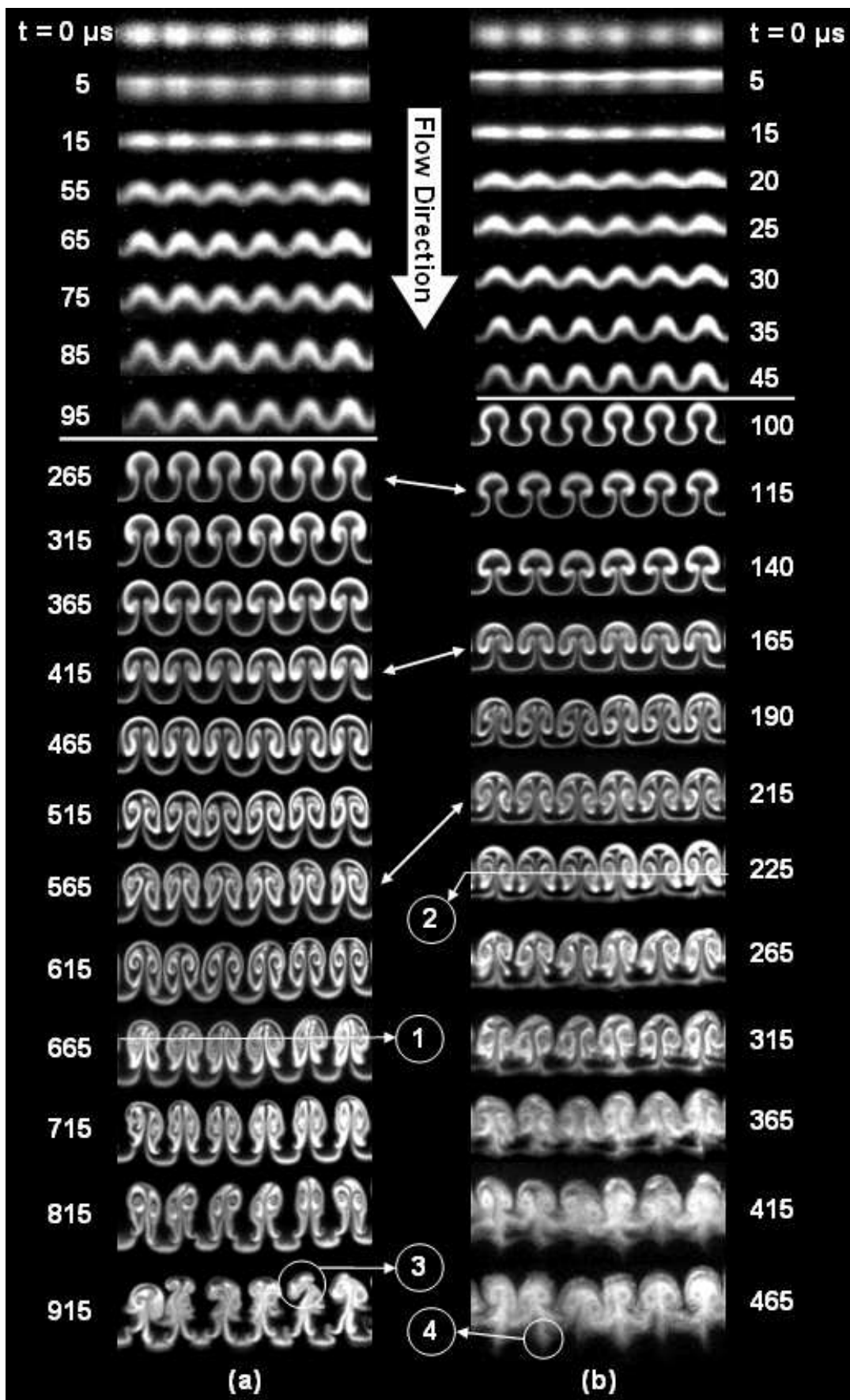
Figure 3.8: Time series for Mach 1.21, (a), and Mach 1.54, (b), with times in $\mu$s. White indicates $SF_6$, while black indicates air. IC's correspond to t=0$\mu$s; shock compression corresponds to 15$\mu$s. Flow is from top to bottom. Lines separating the data show the camera transition from IC to DYN in each data set. Double headed arrows show time comparisons in terms of degree of flow development. 1 and 2 show the average streamwise location of the vortex cores in images for Mach 1.21 and Mach 1.54, respectively, as is discussed in the text. 3 indicates the developement of secondary vortex cores, and 4, the ejected bridge material, as is discussed in the text.
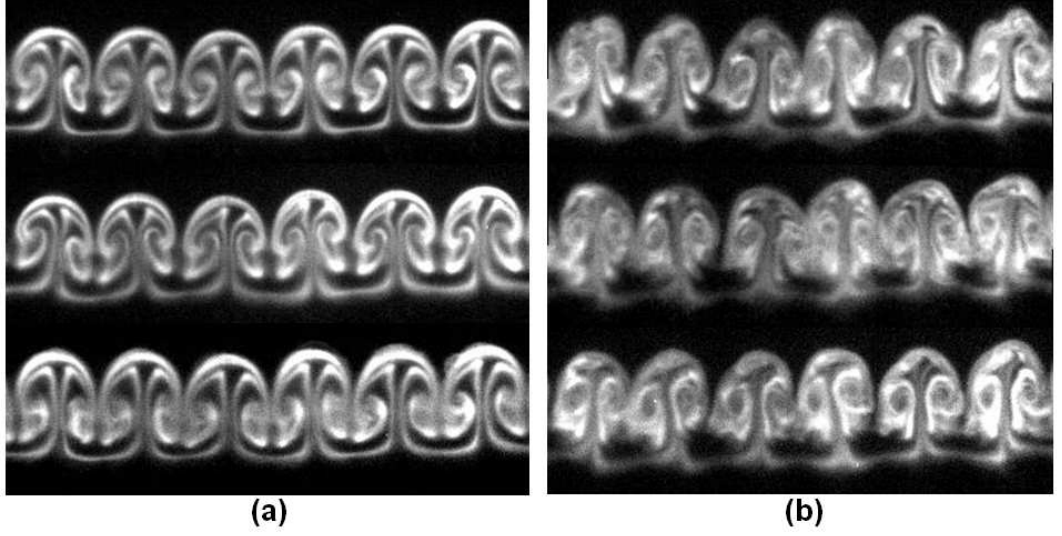
33

Figure 3.9: Illustration of repeatability: (a) three images at 215 $\mu$s after shock impact corresponding to individual runs of the Mach 1.54 experiment; (b) three images at 315 $\mu$s after shock impact corresponding to individual runs of the Mach 1.54 experiment.

for Mach 1.54; and compare t=565$\mu$s for Mach 1.21, and t=215$\mu$s for Mach 1.54. At these earlier time comparisons, many flow features are qualitatively similar, including amount of main vortex roll up, and degree of fluid mixing. The change in time between each of these subsequent comparisons ($\Delta$t=150$\mu$s for Mach 1.21, and $\Delta$t=50$\mu$s for Mach 1.54) indicates that flow structures develop faster in the Mach 1.54 experiment by a factor of 3 in the sense of large scale flow morphology at early times. Subtle differences do exist such as the location of the center of the main vortex with respect to the location of the spanwise center of mass. Figure 3.10 gives a visual description of the flow feature nomenclature used in this report and complements Figure 3.8. Also, in the Mach 1.21 flow morphology, the bridges seem to stretch farther away from the main structure and are more rounded than in the Mach 1.54 morphology.

At late times, however, the evolution of the flow structure diverges markedly between the two experiments, as the more subtle dissimilarities become manifest.
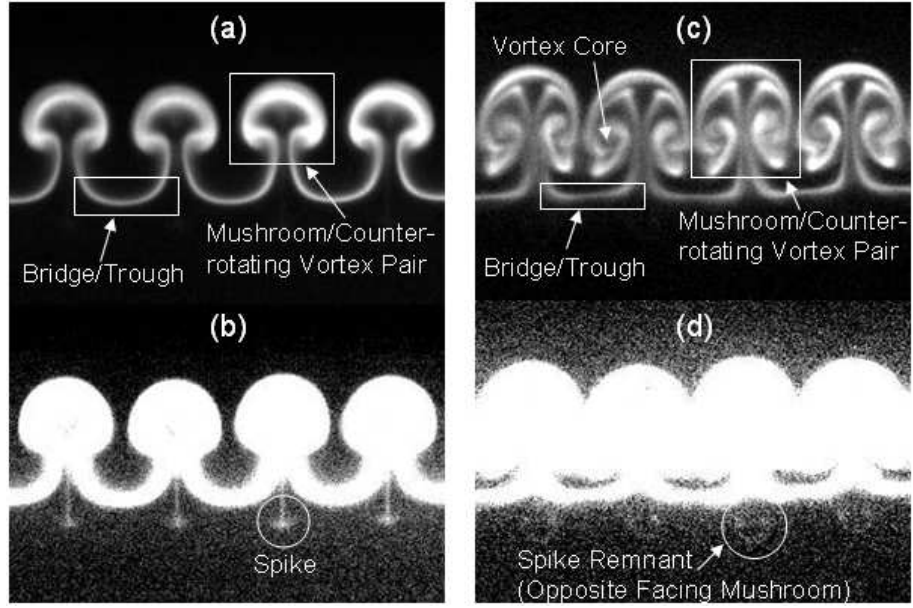
Figure 3.10: Flow feature nomenclature: *Left*: (a)A Mach 1.54 shot at 115$\mu$s, (b)The same shot with contrast adjusted to visualize the spike flow feature; *Right*: (c)A Mach 1.54 shot at 215$\mu$s, (d)The same shot with contrast adjusted to view remnants of spike roll up.

This divergence occurs most prominently, in terms of qualitative flow features, when the Mach 1.21 experiment is at t=715$\mu$s and Mach 1.54 is at t=265$\mu$s. In general, in the Mach 1.21 flow, the individual vortex pairs (mushrooms) remain more spaced throughout their growth, and become more elongated at later times, while the Mach 1.54 vortex pairs appear to grow in the spanwise direction impinging more readily upon one another. Features 1 and 2 in Figure 3.8 illustrate the streamwise location of the vortex cores in a Mach 1.21 and Mach 1.54 image, respectively, for comparison. In the Mach 1.21 image, the vortex cores (identified visually) are located between .6mm and 1mm upstream of the streamwise location of the spanwise–averaged center of mass (determination of center of mass location is discussed below), while in the Mach 1.54 image, the vortex cores are either at the same location as the center of mass, or just slightly above (0.27mm upstream). It is perhaps because the vortex cores are located farther upstream than the center of mass of the structure in the

Mach 1.21 flow that the vortices seem to 'pinch' in the main body of the mushrooms giving rise to feature 3 at t=915$\mu$s, at which time secondary vortex cores appear to have formed.  Contrastingly, at late times in the Mach 1.54 flow, pinching appears to occur at a more downstream location within the structure, keeping the main vortices intact, but causing the material that at earlier times had constituted the bridge to 'protrude' out ahead of the structure.  In this way, the bridge material is pulled toward the middle of the counter rotating vortex pairs, and then squeezed out downstream (feature 4).  In the Mach 1.21 case, the bridge material remains bridge material to the latest accessible time in the experiment, but appears to detach from the mushroom structure between t=715$\mu$s and t=815$\mu$s.  Also, the Mach 1.54 case becomes more well mixed at much earlier times, the onset of which occurs noticeably at t=315$\mu$s, while it is not until the latest time, t=915$\mu$s, that the Mach 1.21 flow reaches a similar degree of mixing.

Based implicitly upon the similarity of the dynamic validation images to those from the earlier data set, the initial conditions between the two experiments correlate well at the scales being investigated in this study.  The similarity of the large-scale features between the two experiments at early time after shock passage also suggests initial condition correlation.  Therefore, it is assumed that the differences between the two experiments in large scale flow features at later times are attributable to Mach number effects resulting from differences in (1) the amount of compression of the initial conditions during shock passage, (2) the amount of vorticity deposited, and (3) the refraction of the incident shock front as it passes through the curtain, and the resulting internal reflections of the shock wave off each interface.  For example, the curtain reaching a more mixed state at earlier times, even if nondimensionalized by the convection velocity, in the higher Mach number experiment is the result of higher vorticity deposited, while differences in the streamwise location of vortex cores relative to the streamwise center of mass probabably results from the geometric differences of shock compression and refraction.

Two experiments were also performed at Mach 2.0 for the first time in this experimental facility. The shots were captured on different days. On one of the days, the dynamic validation images taken at Mach 1.21 were more similar to those from the complete data sets from Figure 3.1. It is this image, taken at t=185$\mu$s after shock impact, which is displayed in Figure 3.11. Also shown in Figure 3.11 for comparison is a shot from the Mach 1.54 data set, at 315$\mu$s, that is similar in overall degree of mixing, and morphology but differs in overall size. The Mach 1.54 shot in Figure 3.11 also differs from the Mach 1.54 image displayed in the time series in Figure 3.8 for the same time after shock impact, demonstrating the degree of variability of data acquired within a given day, but indicating that the initial conditions in the Mach 2.0 shot were similar to that of the complete data sets.
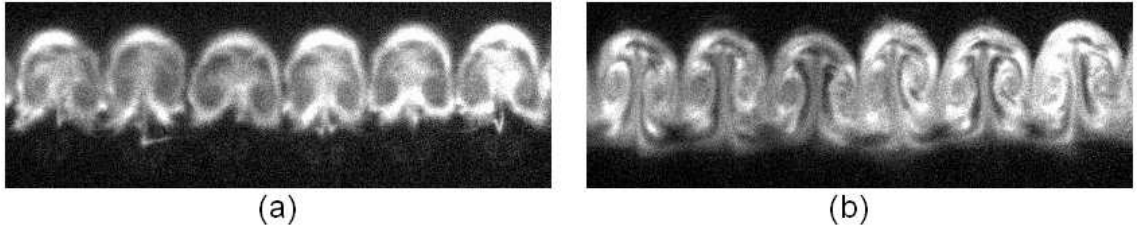


Figure 3.11: (a) A Mach 2.0 shot at 185$\mu$s after shock impact; (b) For comparison, a Mach 1.54 shot at 315$\mu$s with a similar overall flow morphology and degree of mixing.

Another Mach number effect discovered in the current study is the spike feature, defined as the material that ejects (or spikes) out downstream from the center of each mushroom structure at early times, circled in Figure 3.10. It is known that the shock wave front refracts as it passes through the perturbed heavy gas curtain. On the downstream edge of the SF$_6$, the curved shock front focuses as it exits the heavy gas and enters back into the lighter air, producing a larger localized pressure in that region of the heavy gas. The higher pressure causes a small amount of material to spike out ahead of the rest of the structure. This effect and its mechanism were first reported by Kumar *et al.* [32], in which the shock focusing within an 8 mm cylinder is clearly visualized in a Mach 1.2 experiment (see Figure 3.12, reprinted from *Kumar*

*et al.* [32]). In that study, the flow feature under discussion is referred to as a 'cusp' instead of 'spike' (see Figure 3.12 (i)). In the Mach 1.21 data within the current study, the spike is evident at early times, but it is very faint, and in some cases does not jut out far enough to escape getting incorporated with the material behind it as the induced motion of the vortex pair 'swallows' it back up.
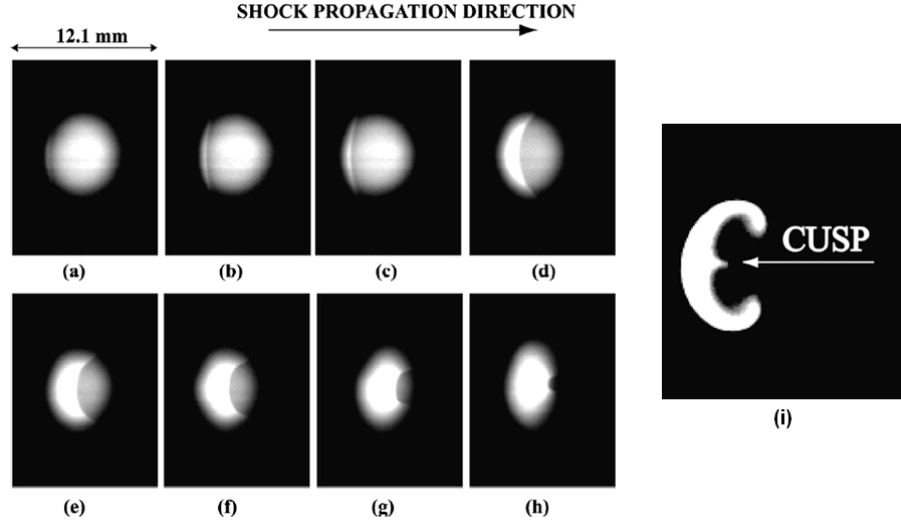


Figure 3.12: From Kumar *et al.* [32], shows shock wave refraction as it passes through an 8mm $SF_6$ cylinder. Flow is from left to right. (a) Shock wave just on upstream edge, t=0$\mu$s; (h) Shock focuses on the downstream edge, t=30$\mu$s; (i) high pressure region on downstream edge causes cusp feature to form, t=130$\mu$s. ((i) is enlarged for visualization)

In both the Mach 1.54 and Mach 2.0 data, the spike portrudes farther away from the main structure, presumably due to the higher pressures involved, and is able to 'escape' being incorporated by the mushroom vortices. With time, the spike itself then rolls up into an opposite facing mushroom, presumably because of viscosity. Because the spike is formed from a small amount of material, the intensity of its PLIF signal is low, and it can be difficult to visualize without changing the contrast of the image as is shown in Figure 3.10. As time increases in the Mach 1.54 data, this material mixes with the surrounding air, thereby decreasing the PLIF signal until there is no evidence of the spike left at the latest times. In the Mach 1.21

experiments, remnants of the spike feature can be seen in some later time images (up to t=415$\mu$s), but no roll up occurs and there is no evidence of an opposite facing mushroom. Over the range of Mach numbers studied, it appears that the higher the Mach number for a given set of initial conditions, the larger the spike, and if applicable, the more prominent the opposite facing mushroom appears to be at later times.

Using the data collected in both Mach 1.21 and Mach 1.54 experiments, streamwise location of center of mass against time was determined. The streamwise center of mass of the curtain within an image was measured by spanwise–averaging intensity over a region of the image chosen to include several wavelengths of the curtain. The average, intensity-weighted, pixel position was then defined to be the center of mass within the image, and an image of a calibration grid was used to map pixel location to downstream position in millimeters. This process was automated and applied to every data point listed in Figure 3.1; results are plotted in Figure 3.13. Center of mass locations of images displayed in the time series (Figure 3.8) are delineated. Best fit lines to the data accumulated by the dynamic camera (DYN) were obtained, giving average convective velocities of 96.4 m/s for Mach 1.21, and 226.4 m/s for Mach 1.54. As can be seen in Figure 3.13, the data all falls very closely onto the best fit lines with little scatter, showing that the convection velocity is constant throughout the experiment despite the generation of vorticity from mechanisms after shock passage. It also indicates that the expansion fan does not reach the test section at any time throughout the duration of the experiment. The small amount of scatter is a further testament to repeatability, and some of the scatter can be explained by small differences in incident shock velocity from one run to the next. In the Mach 1.21 experiments, the incident shock speed varied between 417.47 m/s (Ma=1.207) and 422.93 m/s (Ma=1.222), and in the Mach 1.54 experiments, it varied between 529.15 m/s (Ma=1.529) and 534.69 m/s (Ma=1.545), but these were the outlying shock speeds in each data set and most shots could be rounded to Mach 1.21 or 1.54.
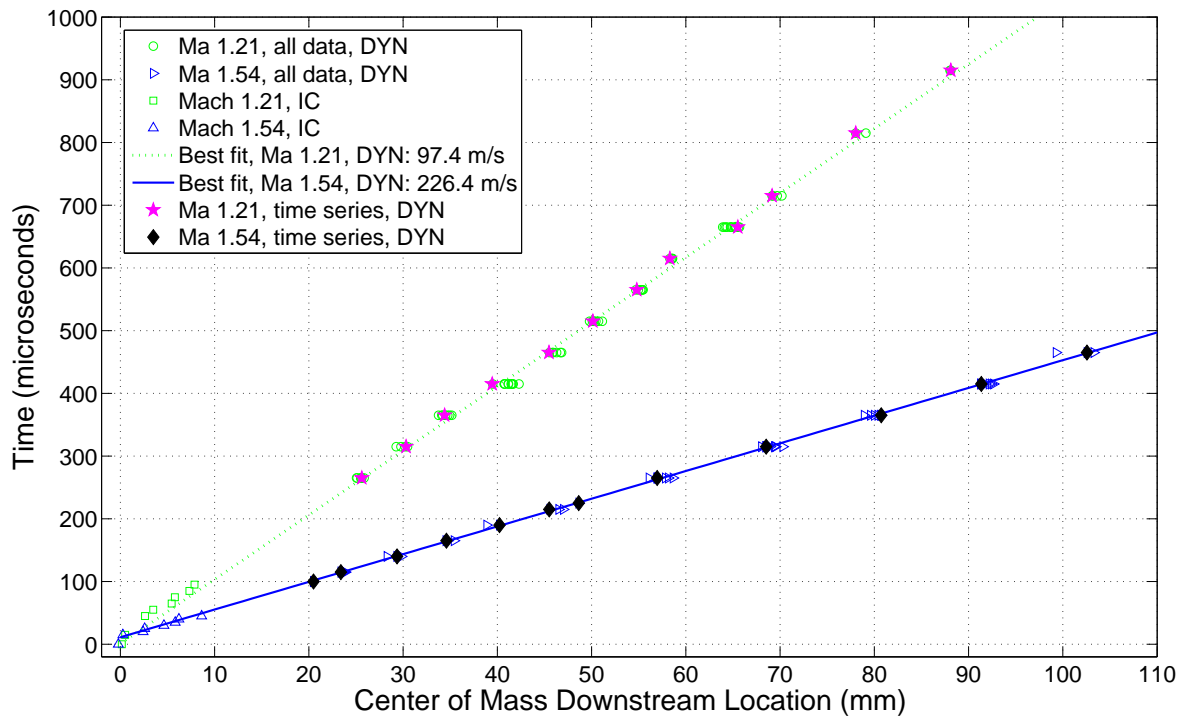
Figure 3.13: Downstream location of center of mass vs time. Linear best fits do not include data points from the IC camera. Based on fits, average convection velocities are 97.4 m/s and 226.4 m/s for Mach 1.21 and Mach 1.54, respectively

## 3.3   Integral Widths

One motivation for the current study was to determine whether perturbation growth rates of experiments at two different Mach numbers could be scaled, or to determine the parameters needed to do so. To this end, quantitative characterization of the data was needed. Integral width, defined as the distance spanning the farthest upstream and downstream location at which $SF_6$ is present (i.e. where there is a PLIF signal) within an individual image, provides a measure of a characteristic large scale in the flow.

While many models exist to predict the perturbation amplitude growth in single interface studies, they are not relevant for prediction of width growth in the current study due to the added level of complexity (two closely spaced interacting interfaces). However, one model for the growth of the mixing width, applicable to the initial conditions in the current study, has been reported previously in literature [35] and has shown good agreement with other varicose curtain experiments [39, 36]. The model is based upon an infinite row of counter-rotating point vortices, each with the same magnitude. An air/$SF_6$ interface is assumed. The input parameters for the model include the circulation, $\Gamma$, the initial width just after shock compression, $w_0$, and a single wave number, $k = \frac{2\pi}{\lambda}$, where $\lambda$ is the wavelength of the perturbations. The equation for the mixing width growth over time according to this model is:

$$w(t) = \frac{2}{k} sinh^{-1} \left[ k^2 \Gamma(t - t_0) + sinh \left( \frac{kw_0}{2} \right) \right] \qquad (3.1)$$

where $t_0$ is the time of the virtual origin of the growth width curve. The virtual origin was not included in the original model, but was added in order to account for any time it may take for phase inversion to occur on the downstream interface between $SF_6$ and air where the shock wave is directed from heavy to light fluid [39, 36]. In the current study, full shock compression is considered to occur at $15\mu$s, so $t_0$ is $15\mu$s

or greater.

To measure integral width consistently, several decisions were made. First, given that the flow is a curtain spanning the width of the test section, the spanwise region over which to make the width measurement was specified. Second, because the PLIF signal from the fluid interface has a finite slope due to mixing and diffusion, a minimum threshold for the $SF_6$ signal was chosen. Third, only the growth of the large-scale vortices were measured so that comparison of the data with the mixing width model is possible until late times. Figure 3.14 gives a visual illustration of the width measurement for two Mach 1.21 images at different times. The integral width of the curtain was measured over one perturbation wavelength at the same spanwise location for each time. Each width was measured by adjusting the contrast of the image and observing a horizontal line profile as it was brought in toward the curtain from either side. When the signal observed in the horizontal line profile first spiked above that of background noise within the spanwise region of measurement, the location was noted, and this was considered the extent of curtain material ($SF_6$). If a spike, or late time remnants of a spike (diffuse opposite facing mushroom) were evident in an image, they were not included in the width measurement as these flow features are not accounted for in the mixing width model. Several attempts were made to remove the subjectivity of these measurements by automating the process. A region of the curtain was selected, spanwise averaged, and then measured for width at some threshold percentage of maximum. While the values attained were similar in scale and trend to those measured by hand, the noise level in the data made the automated process unreliable.

Figure 3.15 shows the mixing width evolution with time for both the Mach 1.21 and Mach 1.54 experiments of Figure 3.1, along with best fit curves to each data set derived from the Jacobs *et al.* mixing width model described above. The images that are displayed in the time series of Figure 3.8 are also delineated. The parameters that
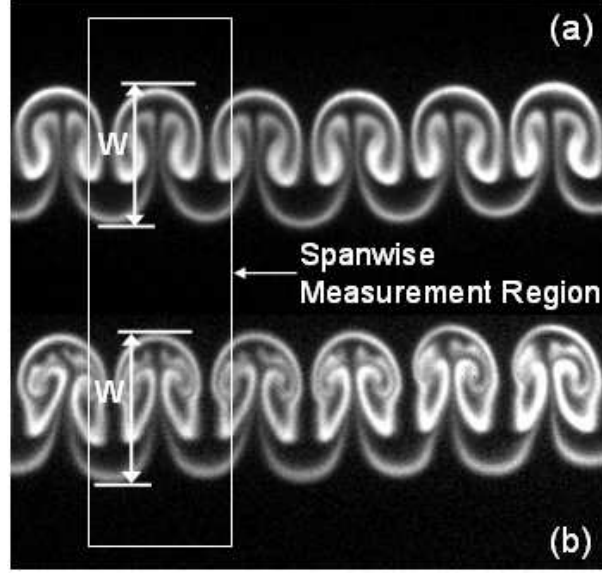
Figure 3.14: Illustration of integral width measurement, $w$, for images from two separate runs of the Mach 1.21 experiment. The box indicates the spanwise region of the image that was considered during the measurement process. (a) t=465$\mu$s; (b) t=565$\mu$s.

were varied to achieve the best fits were the virtual origin, $t_0$, and the circulation, $\Gamma$. Shots in both Mach number experiments were carried out to image the flow just after shock passage, therefore, the initial width, $w_0$, was measured experimentally and fixed. For Mach 1.21, $w_0$= 2.472mm, and for Mach 1.54, $w_0$= 1.693mm. The wave number, $k$, was also measured and fixed at 1.795 mm$^{-1}$. The model curves, with $\Gamma$=0.046 mm$^2$/$\mu$s for Mach 1.21, and $\Gamma$=0.070 mm$^2$/$\mu$s for Mach 1.54, agree very well with the experimental data until late times when the experimental widths grow faster than those predicted by the model. This divergence occurs prominently at 815 $\mu$s for Mach 1.21, and at 415 $\mu$s for Mach 1.54. It is possible that this divergence is a result of increasing flow complexity, and small scale flow features that the model does not have the capacity to incorporate as it assumes completely symmetric, non-diffuse initial conditions, and is inviscid. In the Mach 1.21 data, the discrepancy could be attributed to the mushroom elongation and pinching that creates the secondary vortex pair. In the Mach 1.54 data, it appears to be a result

of the bridge material being induced by the main vortices to protrude out ahead of the rest of the structure. At these late times, the mixing width model appears to be irrelevant.
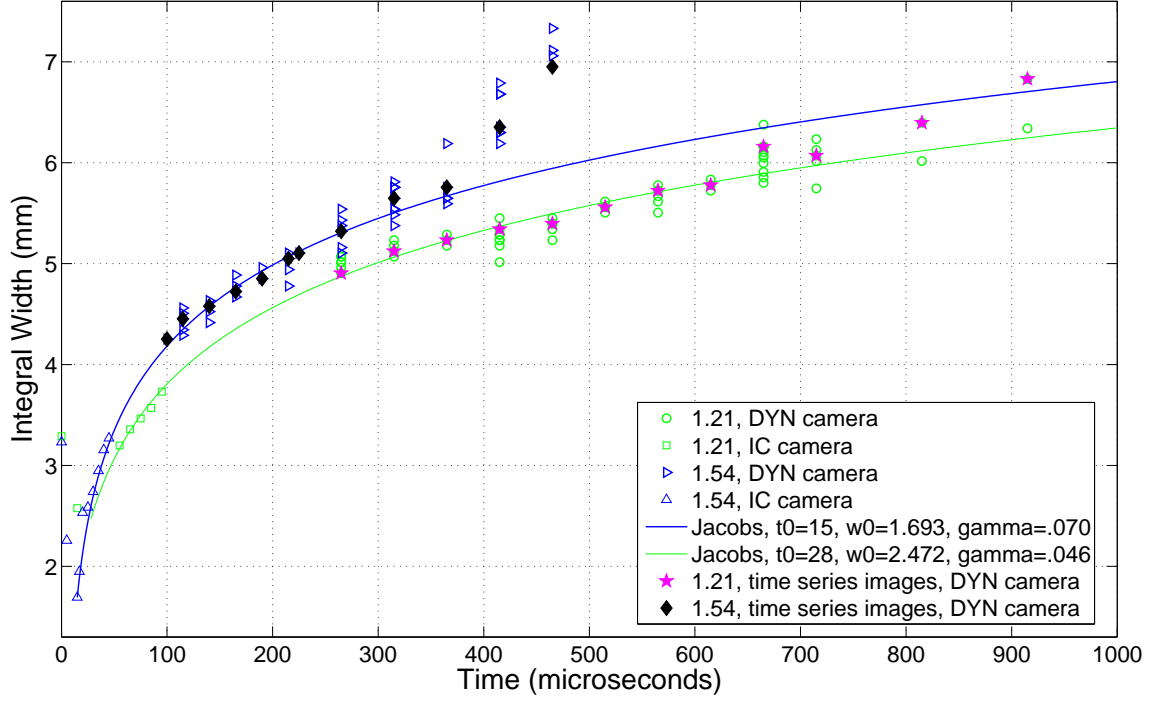


Figure 3.15: Integral Width vs Time; hand measured; Mach 1.21 vs Mach 1.54. The line curves show theoretical width according to the width model discussed in the text: $\Gamma$=.046 mm$^2$/$\mu$s for Mach 1.21, $\Gamma$=.070 mm$^2$/$\mu$s for Mach 1.54. Data points used to create the time series and those captured by the IC camera are delineated.

As was described in Chapter 2, several shots of simultaneous PIV/PLIF data were taken in Mach 1.21 and Mach 1.54 experiments in order to get a combined velocity/density field. Figure 3.16 shows velocity vectors derived from PIV data overlayed upon the corresponding PIV image at t=465$\mu$s in a Mach 1.21 experiment. The velocity field allows for experimental estimation of $\Gamma$ by drawing a closed curve around a region of vorticity and computing the line integral of tangential velocity

along the curve. Using this method, the circulation for Mach 1.21 data and Mach 1.54 data was found to be $.046 \pm .005 \; mm^2/\mu$s and $.095 \pm .010 \; mm^2/\mu$s, respectively. The measured circulation for Mach 1.21 data is the same as that deduced in generating the curve fit in Figure 3.15, adding some validation to the model. However, the measured circulation in the Mach 1.54 case is significantly higher than that used as an input parameter for the curve fit, and the curve generated by the model using this experimental value of circulation does not agree with the data.
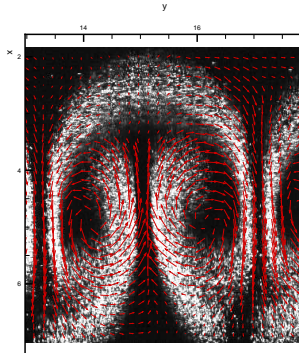


Figure 3.16: An example of PIV in a Mach 1.21 experiment at t=465$\mu$s showing fog droplets with velocity vectors overlaid.

However, it is encouraging that the model can generate curves that agree very well with the measured widths in both Mach number data sets up to later times, albeit with a lower circulation input than the one measured for Mach 1.54. Given this result, the data can be collapsed (until late times) using Equation 3.1 to nondimensionalize based upon some function of the circulation of the best fit curves, and the initial width just after shock compression. This also suggests that the model is only off by a multiplicative factor in the Mach 1.54 case. Nonetheless, the discrepancy of the measured circulation value for Mach 1.54 indicates either that additional parameters are needed to collapse the data meaningfully when Mach number is increased (e.g. diffusion, vortex spacing), or that there were errors in the experimental

measurement of circulation. In the experiment, the air/SF$_6$ interface is diffuse while the model assumes the interface to be sharp. Also, in the experiment, the vortex cores are not perfectly spaced. The distance between the cores of a counter rotating vortex pair (mushroom) is slightly larger than the distance between a vortex core from one mushroom and the nearest vortex core of an immediately adjacent mushroom. In the model, the vortices are evenly spaced. In the Mach 1.21 data set this difference is probably not as important, as the mushrooms remain spaced throughout time. Contrastingly, in the Mach 1.54 experiment, the mushrooms grow more spanwise (relatively) so that they impinge upon one another as mentioned above. This difference may help to explain why there is disagreement in circulation values for Mach 1.54, but good agreement for Mach 1.21 assuming that the experimental estimations of circulation are indeed correct.

Integral mixing width is also plotted against downstream location of the center of mass in Figure 3.17 for the Mach 1.21 and Mach 1.54 experiments listed in Figure 3.1. Images used in the time series of Figure 3.8 are delineated. When this plot was generated, it was recognized that the integral width growth rate appeared to have the same dependence upon downstream location for both Mach 1.21 and 1.54 data sets, with a small offset separating the data vertically. As the growth rate in both data sets appears to be exhibiting asymptotic behavior in the spatial region of the test section captured by the dynamic camera, it is reasonable to use a simple linear fit in order to determine the offset. The incident shock speeds among data used in the time series had less scatter than each respective data set as a whole, so to avoid errors due to small variations in shock speed, only the images used in the time series captured by the dynamic camera were used to find the linear best fits. The best fit linear curves in the form of $y = mx + b$ yielded the same slope (m=0.029 mm/mm) for both data sets, with b= 4.17 mm and 3.68 mm for Mach 1.21 and 1.54, respectively. When this offset ($\Delta$b=0.49 mm) is added to the integral widths of the Mach 1.54 data, all of the data collapses well. Figure 3.18 shows the integral mixing
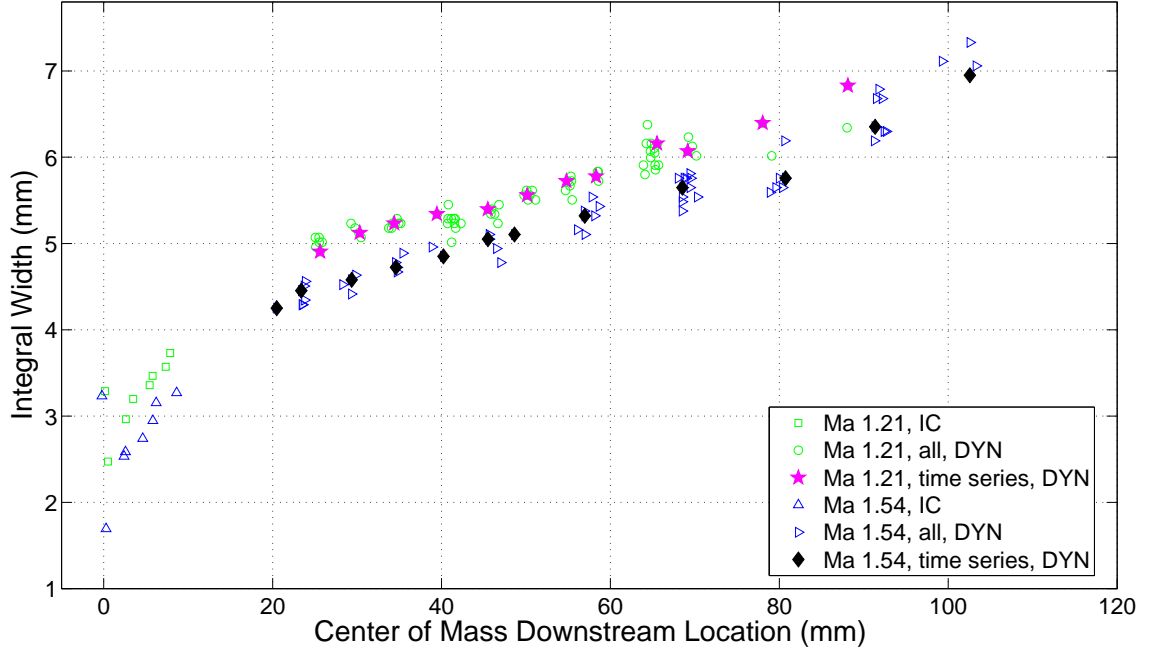
Figure 3.17: Integral width vs downstream location of center of mass; Mach 1.21 vs Mach 1.54. Data points used to create the time series and those captured by the IC camera are delineated.

width plotted against downstream location with $\Delta b$=0.49 mm added to the Mach 1.54 data; for clarity, only images used in the time series in Figure 3.8 are plotted in Figure 3.18 to illustrate the data collapse. On average, the integral width grows 0.029 mm for every 1 mm that the curtain travels for the downstream region captured by the dynamic camera (20.49mm $\leq$ x $\leq$ 103.30mm), independent of the shock wave Mach number. Unfortunately, there is a region of downstream location that could not be visualized in the experiment between imaging views of the IC camera and the dynamic camera (8.63mm < x < 20.49mm), and it appears that it is in this spatial region that the growth rate changes most dramatically.

Plotting integral width against downstream location has the same effect as nor-
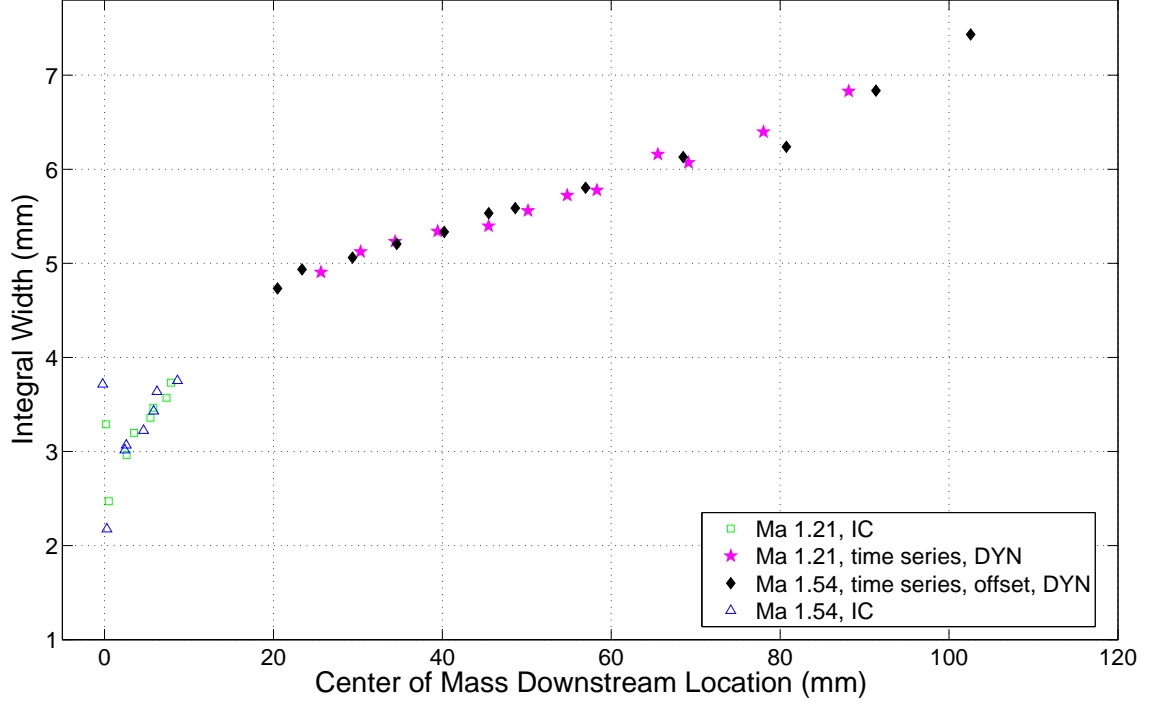
Figure 3.18: Integral width vs downstream location of center of mass, with the offset, .49mm, added to the Mach 1.54 data. For clarity of presentation, for the data captured by the dynamic camera, only the images used in the time series are displayed.

malizing time with the respective convection velocity of every run of the experiment. This normalization, in addition to the offset, appear successful for integral width data collapse between experiments at different Mach numbers, given the initial conditions in the current study. It is conjectured that the offset needed to collapse the data has a physical basis in the difference between post-shock compression widths ($\Delta w_0$), as $\Delta w_0$=0.779 mm (measured in the experiment) and $\Delta b$=0.49 mm are on the same order ($\Delta b$=0.63*$\Delta w_0$). Whether using convection velocity for normalization, and an offset related to post-shock compression width is sufficient for collapse of integral growth width for a wide range of Mach number experiments, given the initial conditions in the current study, remains an object of further study, but it appears adequate here without need for additional parameters.

# Chapter 4

# Conclusions

## 4.1 Summary of Results

Experimental results are reported characterizing the Richtmyer-Meshkov instability of a varicose perturbed heavy gas curtain after it is impulsively accelerated by shock waves of varying Mach numbers. Qualitative PLIF was used to obtain maps of $SF_6$ concentration before shock impact and at various times there after. Pressure traces from example runs of the experiment at each Mach number are in good agreement with theoretical X-T diagrams. Initial condition repeatability was demonstrated, and allows for the tracking of many flow features through time despite only capturing one dynamic image for each run of the experiment.

A time series of twenty PLIF images was constructed for both the Mach 1.21 and the Mach 1.54 data, allowing for qualitative comparison of the post-shock flow evolution in each case. Although the large scale flow morphology is similar at early times, several qualitative flow features are identified that are considered to be the result of Mach number effect. At early times these features include: (1) development of the R-M instability occurs faster in Mach 1.54 experiments (perhaps by a factor

of three), (2) the shape of the bridge material is flattened in Mach 1.54 experiments compared to those at Mach 1.21, (3) the streamwise location of the vortex cores relative to the spanwise averaged center of mass is farther upstream in Mach 1.21 experiments compared to those at Mach 1.54, (4) the spike feature is more prominent with increasing Mach number, and can roll up to form an opposite facing mushroom if Mach number is high enough.

At later times, differences in flow features attributed to Mach number effect include: (5) vortex cores become mixed much faster in real time with increasing Mach number, (6) the mushrooms are remain spaced more widely and become more elongated in the Mach 1.21 experiments, while mushrooms grow more spanwise in those of Mach 1.54, (7) bridge material in Mach 1.54 experiments is induced by the main vortex cores to move to the spanwise center position of each counter-rotating vortex pair in time, while in Mach 1.21, bridge material remains intact throughout time, (8) vortex 'pinching' in Mach 1.21 leads to the development of secondary vortex cores, while in Mach 1.54, it leads to the downstream protrusion of what was formerly bridge material.

Additionally, analysis of a quantitative flow feature, integral mixing width, shows that integral width growth rate with time is higher in Mach 1.54 experiments than in those of Mach 1.21. A plot of mixing width vs time is presented, along with best fit curves generated using the Jacobs *et al.* [35] mixing width model varying the circulation parameter. The best fit curves showed good agreement to the experimental data until late times ($\approx 815\mu$s for Mach 1.21, and $\approx 415\mu$s for Mach 1.54), when the vortex 'pinching' mechanism creates abnormalities in late–time flow behavior. Experimental values of circulation were calculated from experimental runs that used simultaneous PIV/PLIF imaging techniques yielding two-dimensional velocity and density maps at the same time within the same individual run of the experiment. It was found that the measured circulation is in excellent agreement with that of the

best fit curve for the Mach 1.21 experiment (.046 mm$^2$/$\mu$s). The measured circulation for Mach 1.54 experiments (.095 $\pm$ .010mm$^2$/$\mu$s) is not in particularly good agreement with that of the best fit curve (.070 mm$^2$/$\mu$s). Because the mixing width model is able to produce curves that match the trends in the experimental data, the model is partially validated for early times, and the data can be collapsed using the equation and parameters from the model. However, due to the discrepancy of circulation values in the Mach 1.54 case, such a collapse is not necessarily meaningful in a strictly physical sense.

A plot of integral mixing width vs. downstream location is also presented. Plotting width against downstream location has the same effect on data trends as normalizing time based upon the convection velocity of the interface. This plot shows that the trend in layer width over distance travelled is the same for both Mach 1.21 and Mach 1.54 data sets. This similarity was confirmed by finding that linear best fits to the data at intermediate to late time yield the same slope. Note that fitting the data to a linear function is not intended to demonstrate that the width growth rate is constant in nature; indeed, the R-M instability is in a nonlinear regime in this study (the amplitude of perturbations is on the same scale or larger than the wavelength, 3.5 mm, and the two interfaces are interacting). However, it does help demonstrate that the growth rate with respect to distance travelled is the same for both experiments, on average. The appearance of an approximately linear trend is more likely the result of aymptotic behavior, as the width growth rate is higher in the early time data taken by the IC camera. It is suggested that the small vertical (integral width) offset in the two data sets can be attributed to the difference in post-shock compression as a result of different strength incident shock waves. Hence, in this study it is found that only two parameters are needed for collapse of the integral mixing width data: the convection velocity imparted upon the curtain by the incident shock wave, and the width of the post-shock, compressed initial conditions.

## 4.2 Future Work

Accumulating complete data sets at additional Mach numbers (e.g., Mach 2.0) would represent a natural progression of the work reported here. In this way, one could help determine if integral width growth rate with respect to distance travelled is independent of Mach number, as presently suggested, or if the findings of the current study were specific to the experiment. Transitions in flow morphology with increasing Mach number may also be determined, as well as other Mach number effects. It may also be useful to carry out such experiments with different initial conditions. A small heavy gas cylinder (3 mm in diameter) may be an ideal test case for its repeatability. The mass flow rate is much smaller in a 3 mm cylinder than in the varicose curtain, promoting laminar flow, and adding more reproducibility to the post-shock flow evolution.

Pursuit of other measures by which to characterize the data may also prove useful. Integral mixing width provides one measure that accounts for the flow on the largest scale, but analysis of smaller scale characteristics of the flow could be enlightening. For example, one may investigate the mixing rate parameter, $\chi$ [43], to understand the time dependence of mixing rate for comparison between experiments at different Mach numbers.

In future experiments, the initial condition camera should be stabilized so that initial conditions can be correlated quantitatively. Also, additional investigation of the intrusiveness of initial condition imaging using PLIF is needed to understand the mechanism by which it occurs so that it can perhaps be mitigated.

# Appendices

# Appendix A

# Effect of PLIF Imaging on the Initial Conditions

Several experiments were performed to investigate the impact of the PLIF laser on the initial conditions, and thus the resulting flow. It was determined that if the PLIF laser power was high enough, and if the initial conditions were pulsed shortly before shock arrival, image blurring at subsequent dynamic times occurred (see Figure A.1 for a visual illustration). In general, the later the time, the higher the Mach number, and the higher the laser power, the more prominent the image blurring, as changes imposed by the laser upon the IC's get amplified over time. Interestingly, if the laser is pulsed just after shock passage or any time thereafter, no image blurring in dynamic images is observed, independent of laser power. Also, no image blurring is observed when the IC pulse power is sufficiently low. Although it appears that the IC laser pulse, when at high power and focused into a thin sheet, alters the initial conditions in some way, it remains inconclusive whether it is the $SF_6$ that is altered, or if it is only the acetone vapor seeding. Uneven heating leading to an alteration of density gradients is one possible mechanism that can be explored. It is also not known whether the effect has a threshold at some laser power intensity,

below which no blurring occurs, or if it is continuous with laser power intensity, and that no blurring is observed when operating at low power because the effect is small. In order to mitigate this effect, as mentioned in the text, the power of the IC pulse was lowered until no image blurring could be observed in dynamic images, and in subsequent experiments operation was kept in this low power regime. Lowering the IC laser pulse from maximum to a sufficiently low power lowered the signal to noise ratio of the initial conditions from 14 to 4. Further study is needed to understand the mechanism that causes this image blurring effect, as its consequences could be important to many experiments that use PLIF diagnostics.
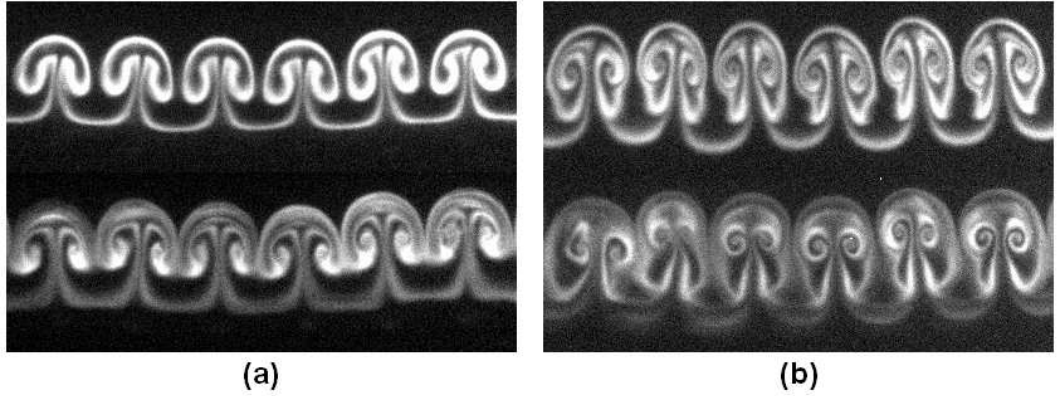


Figure A.1: (a) *Top*, An image from a Mach 1.54 experiment taken at t=215$\mu$s; without pulsing the initial conditions, *bottom* an image from a different Mach 1.54 experiment at the same time with nominally the same initial conditions, but imaged with the IC laser pulse at maximum power; note the apparent blurring of material lines. (b) *Top*, An image from a Mach 1.21 experiment taken at t=615$\mu$s; without pulsing the initial conditions, *bottom* an image from a different Mach 1.21 experiment at the same time with nominally the same initial conditions, but imaged with the IC laser pulse at maximum power; note the apparent blurring of material lines.

# References

[1] R. D. Richtmyer, *Taylor instability in shock acceleration of compressible fluids*, Communications on Pure and Applied Mathematics **13** (1960), 297–319.

[2] Y. Y. Meshkov *Instability of a shock wave accelerated interface between two gases* Technical Report NASA TT F-13074, NASA Technical Translation (1970).

[3] M. Brouillette, *The Richtmyer-Meshkov instability*, Annual Review of Fluid Mechanics **34** (2002), 445–468.

[4] L. Rayleigh, *The Scientific Papers of Lord Rayleigh*, Vol. 2, Cambridge University Press (1900), Cambridge.

[5] G. Taylor, *The instability of liquid surfaces when accelerated in a direction perpendicular to their planes*, Proceedings of the Royal Society of London Series A **201** (1950), 192–196.

[6] C. E. Niederhaus and J. W. Jacobs, *Experimental study of the richtmyer-meshkov instability of incompressible fluids*, Journal of Fluid Mechanics **485** (2003), 243–277.

[7] W. Hogan, R. Bangerter, and G. Kulcinski, *Energy from inertial fusion*, Physics Today **45** (1992), 42–50.

[8] B. D. Collins and J. W. Jacobs, *PLIF flow visualization and measurements of the Richtmyer-Meshkov instability of an air/SF$_6$ interface*, Journal of Fluid Mechanics **464** (2002), 113–136.

[9] M. Brouillette and B. Sturtevant, *Growth induced by multiple shock waves normally incident on plane gaseous interfaces*, Physica D **37** (1989), 248–263.

[10] I. Currie, *Fundamental Mechanics of Fluids*, Third edition, New York: Marcel Dekker, Inc., 2003 (65-66, 448-449).

*References*

[11] N. J. Zabusky, *Vortex paradigm for accelerated inhomogeneous flows: visiometrics for the Rayleigh-Taylor and Richtmyer-Meshkov environments*, Annual Review of Fluid Mechanics **31** (1999), 495–536.

[12] A. Rikanati, D. Oron, O. Sadot, and D. Shvarts, *High initial amplitude and high Mach number effects on the evolution of the single-mode Richtmyer-Meshkov instability*, Physical Review E **67** (2003), 026307.

[13] O. Sadot, A. Rikanati, G. Ben-Dor, and D. Shvarts, *An experimental study of the high Mach number and high initial-amplitude effects on the evolution of the single-mode Richtmyer-Meshkov instability*, Laser and Particle Beams **21** (2003), 341–346.

[14] O. Sadot, K. Levy, A. Yosef-Hai, D. Cartoon, Y. Elbaz, Y. Srebro, G. Ben-Dor, and D. Shvarts, *Studying hydrodynamic instability using shock-tube experiments*, Astrophysics and Space Science **298** (2005), 305–312.

[15] O. Sadot, L. Erez, U. Alon, D. Oron, L. Levin, G. Erez, G. Ben-Dor, and D. Shvarts, *Study of nonlinear evolution of single-mode and two-bubble interaction under Richtmyer-Meshkov instability*, Physical Review Letters **80** (1998), 1654–1657.

[16] M. V. Bliznetsov, N. V. Nevmerzhitsky, A. N. Rasin, E. A. Sotskov, E. D. Senkovsky, L. V. Tochilina, and V. A. Ustinenko, *Study of turbulent mixing development at the gas-gas interface of shock wave at Mach numbers from 2-9*, in AIP Conference Proceedings, (E. Avrorin and V. Simonenko, eds.), Vol. 849 American Institute of Physics, 2006, pp. 341–346.

[17] J. F. Haas and B. Sturtevant, *Interaction of weak shock waves with cylindrical and spherical gas inhomogeneities*, Journal of Fluids Mechanics **181** (1987), 41–76.

[18] D. A. Holder, A. V. Smith, C. J. Barton, and D. L. Youngs, *Shock-tube experiments on Richtmyer-Meshkov instability growth using an enlarged double-bump perturbation*, Laser and Particle Beams **21** (2003), 411–418.

[19] R. Bonazza and B. Sturtevant, *X-ray measurements of growth rates at a gas interface accelerated by shock waves*, Physics of Fluids **8** (1996), 2496–2512.

[20] P. B. Puranik, J. G. Oakley, M. H. Anderson, and R. Bonazza, *Experimental study of the Richtmyer-Meshkov instability induced by a Mach 3 shock wave*, Shock Waves **13** (2004), 413–429.

## References

[21] M. A. Jones and J. W. Jacobs, *A membraneless experiment for the study of Richtmyer-Meshkov instability of a shock-accelerated gas interface*, Physics of Fluids **9** (1997), 3078–3085.

[22] J. W. Jacobs and V. V. Krivets, *Experiments on the late-time development of single-mode Richtmyer-Meshkov instability*, Physics of Fluids **17** (2005), 034105.

[23] J. W. Jacobs and J. M. Sheeley, *Experimental study of incompressible Richtmyer-Meshkov instability*, Physics of Fluids **8** (1996), 405–415.

[24] R. F. Benjamin and J. N. Fritz, *Shock loading a rippled interface between liquids of different densities*, Physics of Fluids **30** (1987), 331–336.

[25] R. L. Holmes, G. Dimonte, B. Fryxell, M. L. Gittings, J. W. Grove, M. Schneider, D. H. Sharp, A. L. Velikovich, R. P. Weaver, and Q. Zhang, *Richtmyer-Meshkov instability growth - experiment, simulation and theory*, Journal of Fluid Mechanics **389** (1999), 55–79.

[26] G. Dimonte and B. Remington, *Richtmyer-Meshkov experiments on the NOVA laser at high compression*, Physical Review Letters **70** (1993), 1806–1809.

[27] D. Ranjan, M. Anderson, J. Oakley, and R. Bonazza, *Experimental investigation of a strongly shocked gas bubble*, Physical Review Letters **94** (2005), 184507.

[28] D. Ranjan, J. Niederhaus, B. Motl, M. Anderson, J. Oakley, and R. Bonazza, *Experimental investigation of primary and secondary features in high-Mach-number shock-bubble interaction*, Physical Review Letters **98** (2007), 024502.

[29] J. Jacobs, *The dynamics of shock accelerated light and heavy gas cylinders*, Physics of Fluids A **5** (1993), 2239–2247.

[30] C. D. Tomkins, K. P. Prestridge, P. M. Rightley, P. V. Vorobieff, and R. F. Benjamin, *Flow morphologies of two shock-accelerated, unstable gas cylinders*, Journal of Visualization **5** (2002), 273–283.

[31] C. Tomkins, K. Prestridge, P. Rightley, M. Marr-Lyon, P. Vorobieff, and R. Benjamin, *A quantitative study of the interaction of two Richtmyer-Meshkov-unstable gas cylinders*, Physics of Fluids **15** (2003), 986–1004.

[32] S. Kumar, G. Orlicz, C. Tomkins, C. Goodenough, K. Prestridge, P. Vorobieff, and R. Benjamin, *Stretching of material lines in shock-accelerated gaseous flows*, Physics of Fluids **17** (2005), 082107.

*References*

[33] J. W. Jacobs, D. L. Klein, D. G. Jenkins, , and R. F. Benjamin, *Instability growth patterns of a shock-accelerated thin fluid layer*, Physical Review Letters **70** (1993), 583–586.

[34] J. M. Budzinski, R. F. Benjamin, and J. W. Jacobs, *Influence of initial conditions on the flow patterns of a shock-accelerated thin fluid layer*, Physics of Fluids **6** (1994), 3510–3512.

[35] J. Jacobs, D. Jenkins, D. Klein, and R. Benjamin, *Nonlinear growth of the shock-accelerated instability of a thin fluid layer*, Journal of Fluid Mechanics **295** (1995), 23–42.

[36] P. M. Rightley, P. Vorobieff, and R. F. Benjamin, *Evolution of a shock-accelerated thin fluid layer*, Physics of Fluids **9** (1997), 1770–1782.

[37] P. M. Rightley, P. Vorobieff, R. Martin, and R. F. Benjamin, *Experimental observations of the mixing transition in a shock-accelerated gas curtain*, Physics of Fluids **11** (1999), 186–200.

[38] K. Prestridge, P. M. Rightley, P. Vorobieff, R. F. Benjamin, and N. A. Kurnit, *Simultaneous density-field visualization and PIV of a shock-accelerated gas curtain*, Experiments in Fluids **29** (2000), 339–346.

[39] K. Prestridge, P. Vorobieff, P. M. Rightley, and R. F. Benjamin, *Validation of an instability growth model using particle image velocimetry measurements*, Physical Review Letters **84** (2000), 4353–4356.

[40] P. Vorobieff, P. M. Rightley, and R. F. Benjamin, *Shock-driven gas curtain: fractal dimension evolution in transition to turbulence*, Physica D **133** (1999), 469–476.

[41] K. O. Mikaelian, *Numerical simulations of Richtmyer-Meshkov instabilities in finite-thickness fluids layers*, Physics of Fluids **8** (1996), 1269–1292.

[42] R. Bonazza, *Wisconsin shock tube laboratory*, University of Wisconsin. Online (2004). (http://silver.neep.wisc.edu/∼shock/).

[43] C. Tomkins, S. Kumar, G. Orlicz, and K. Prestridge, *An experimental investigation of mixing mechanisms in shock-accelerated flow*, Journal of Fluid Mechanics (submitted for review).